Crack on a chip test method for thin freestanding films

S. Jaddi, M. Coulombier, J.-P. Raskin[+], T. Pardoen

Institute of Mechanics, Materials and Civil Engineering, Université catholique de Louvain, 1348 Louvain-la-Neuve, Belgium

[+]*Institute of Information and Communication Technologies, Electronics and Applied Mathematics, Université catholique de Louvain, 1348 Louvain-la-Neuve, Belgium*

Abstract

Fracture mechanics has been applied for more than two decades to various crack configurations in films on substrate. Fracture toughness data are indeed needed for the design and integrity assessment of many coatings and microelectronics devices. Nevertheless, it is sometimes complicated to deconvolute the constraint exerted by the substrate on the cracking process especially in the presence of viscoelastic or plastic dissipation. Here, a new on chip test method has been developed to determine the fracture toughness of freestanding submicron films. Beside the advantage of avoiding the constraint induced by the substrate, freestanding films allow, if sufficiently thin, direct observation of the fracture mechanisms by transmission electron microscopy. The design of this new nano(micro)-testing consists of two long actuator beams undergoing large internal stress. A specimen is attached to these two actuators, incorporating a notch produced by lithography. Two types of geometries are addressed, one being a double cantilever beam type configuration, while the other is a center cracked panel. Both actuators and specimen are deposited on a sacrificial layer. The etching of the sacrificial layer induces the release of the test structure, with the actuators then contracting and pulling on the test specimen. A crack is initiated from the notch tip, propagates and finally stops when the energy release rate has decreased down to its critical value. This crack arrest measurement avoids the problem of introducing a sufficiently sharp precrack. Analytical equations that describe the stress intensity factor as a function of the geometrical characteristics of the test structures are worked out to guide the dimensional analysis. Extensive finite element analysis provides the full parameter variations necessary to quantify the fracture toughness from experimental data and to capture the process of initiation, unstable cracking and arrest followed by possible further stable propagation. For the sake of a proof of concept, ~50 and ~100 nm-thick silicon nitride films produced by low pressure chemical vapor deposition were tested, leading to a mean fracture toughness equal to ~2 MPa$\sqrt{\text{m}}$.

Keywords: Fracture toughness; Residual stress; Thin films; Silicon nitride; On-chip mechanical testing; Finite element (FE).

1. Introduction

The evaluation, control and improvement of the fracture resistance of thin film materials and coatings is a major concern: (i) in microelectronic devices where thermomechanical loading and size reduction lead to a realm of failure issues; (ii) in flexible electronics systems where electrical conductivity must be maintained without cracking under large distortions; (iii) in functional coatings where optimum performance often requires the absence of cracks; (iv) in protective coatings where corrosion, scratch, erosion and wear are partly controlled by the cracking resistance; (v) in thin membrane technologies, such as purification membranes, where cracking is prohibited; (vi) in biology, biomaterials and living tissues where cracking constitutes an injury. In all these applications, cracking results from a combination of externally applied loadings, thermal mismatch effects and other sources of internal stress. As a starting point to guide the design of failsafe thin film solutions, the relevant fracture toughness parameters must be determined, i.e. the critical stress intensity factors for each mode K_{Ic}, K_{IIc}, K_{IIIc} or a mode dependent G_c. The objective is, first, to allow comparing systems among one another and, second, to assess their integrity under loading. The question of interface fracture resistance is also essential for most applications indicated above, although out of the scope of the present study.

While many methods have been proposed to extract the fracture resistance of thin films and coatings on substrate, there are several reasons which motivate the development of robust test methods applicable to freestanding films. The main motivation to look at cracking in freestanding films is to avoid substrate effects. Indeed, in a film-on-substrate configuration, deconvolution of substrate effects from the intrinsic fracture resistance of the film is often not straightforward. The energy release rate associated to a crack propagating in a film on a substrate is given by (Hutchinson and Suo, 1992)

$$G = \frac{Z\sigma^2 h_f}{E_f^*}, \tag{1}$$

where E_f is the elastic modulus of the film (with $E_f^* = E_f/(1-\nu_f^2)$ in plane strain and $E_f^* = E_f$ in plane stress), σ is the stress in the film, h_f is the thickness of the film, and Z is dimensionless constant that is dependent, among others, on the Dundurs' elastic mismatch parameters. The substrate effect enters through the magnitude of the factor Z which has been tabulated for elastic substrates (e.g. Hutchinson and Suo, 1992, Beuth et al., 1992). However, if plastic deformation develops in the substrate due to the high local stress concentration or if viscoelastic dissipation takes place, the impact on the magnitude of G is more complicated to quantify, see for instance the recent work by Kim et al. (2016). Also, in the case of equibiaxial internal stress, the crack can undergo significant loading parallel to the crack propagation

direction. For these reasons, robust fracture mechanics test methods for freestanding films are heavily needed at least to complement film-on-substrate based methods.

For layers that are typically thicker than ~10 micrometers, standard fracture mechanics methods can be used to test freestanding sheets, assuming that the layers can be made freestanding. Care should just be taken in the fatigue pre-cracking process and in sample manipulation to avoid unwanted distortions but, otherwise, macroscopic procedures can be used.

For thinner layers in the micron or submicron thickness regime, difficulties accumulate in terms of manipulation, precracking, load application, detection of cracking initiation, measurement of extremely small load, etc. Several approaches have been proposed to address these challenges and to determine valid fracture toughness of freestanding submicron films. This involves microtensile test configurations (Bellante et al., 2005, Jonnalagadda et al., 2008), bending tests (Jiang et al., 2000, Massl et al., 2009) or bulge tests (Xiang et al., 2005, Merle and Goken, 2011). Different initial defect geometries have been investigated as well. Ballarini and Kahn (Ballarini et al., 1997, Kahn et al., 1999) looked at the fracture toughness using micromachined notched specimens under tensile loading applied on chip. Other researchers developed techniques requiring the use of external loading set up to induce the fracture of notched samples. For instance, Sharpe et al. (1997), Tsuchiya et al. (1997) performed in-situ characterizations on notched samples produced by photolithography and Iqbal et al. (2012) on notched samples produced by Focused Ion Beam (FIB). Perforated specimens were tested by Chasiotis and Knauss (2003a, 2003b) using a tensile loading device. The holes with elliptical shape act as notches involving relatively large radius of curvature. The question comes whether a notched specimen can provide a valid fracture toughness value.

A precrack is considered as sufficiently sharp in the context of fracture mechanics if the initial crack tip opening (CTOD) is smaller than the critical crack tip opening displacement δ_c. The δ_c is on the order of G_c/σ_0. In thin films, the expected fracture toughness G_c ranges between ~1 and 20 J/m^2. For hard films σ_0 is larger than 1 GPa and sometimes much larger, hence δ_c is on the order or below 1 nm. For more ductile metallic films σ_0 is around a few hundreds MPa of larger (this relatively high yield strength compared with bulk metals is a result from the nanocrystalline structure), hence δ_c is typically around 10 to 50 nm. Producing precracks with initial opening smaller than the values indicated above by FIB or by electron beam lithography (e-beam) is impossible, especially for brittle materials. Furthermore, FIB is known to introduce defects which will affect the response of the fracture process zone at cracking initiation. To our knowledge, the only reported technique which allows generating perfectly sharp precrack in the sense of fracture mechanics is by inducing an indentation crack as first applied by Kahn et al. (2000) though suggested earlier by Keller (1998). The indentation is made in a brittle substrate very close to the specimen, which is still lying on the substrate with the crack propagating and penetrating into the specimen. Polycrystalline silicon (poly-Si)

specimens were loaded using electrostatic actuators produced on the same chip. Chasiotis et al. (2006) worked out another indentation induced precracking technique to test poly-Si films via an external microtensile tester. One of the drawbacks of this technique is that the specimen must be very well aligned with the loading apparatus. Similarly, Espinosa and Peng (2005) developed a membrane deflection fracture test method applied to specimens involving an indentation precrack. This elegant precracking method works for sufficiently brittle systems only (Li and Bhushan, 1998). It is quite difficult to control in order to generate a crack with the expected size and orientation.

The objective of the present work is to develop a versatile fracture mechanics test method for freestanding films. The technique relies on several principles that will be further developed in the paper:

1. Work with a crack arrest configuration. The idea is to start with a notch made by lithography methods, to initiate and to propagate a crack until it arrests.
2. Use MEMS-based methods to deposit and pattern the specimens directly on the test device in order to avoid manipulation and transfer which could potentially lead to undesirable damage. This also allows producing a large number of specimens hence possibly providing statistically representative data.
3. Apply the load on chip to avoid connecting to an external macroscopic or microscopic device.

In order to meet these objectives, we have extended a concept of internal stress driven nanotest structures developed over the last 10 years (e.g. Fabrègue et al. 2007, Gravier et al. 2009, Coulombier et al. 2010, Bhaskar et al. 2012, Vayrette et al. 2015, Pardoen et al. 2016) to produce the configurations shown in Figure 1a. These test structures are fabricated following the steps schematically illustrated in Fig. 1b. The principle is to start by depositing a sacrificial layer onto a Si wafer. Then, a layer with high internal tensile stress is deposited and patterned by lithography in the form of two "actuator" beams. The specimen is deposited next and patterned as a long rectangular beam with a notch in the center. By etching the sacrificial layer, the actuator beams contract, acting like springs, to impose a displacement to the test sample. If the imposed displacement is large enough, a crack will be initiated at the notch tip. The crack propagates and then arrests at some distance from the original notch, with a total crack length a. By mechanical analysis of the test configuration, one can relate the final crack length to the applied K_I value, which is equal to the fracture toughness K_{Ic} assuming the arrest toughness is equal to the initiation toughness. The magnitude of K_I will depend on the internal stress level in the beam and on the dimensions of the test structures.

This paper describes in details the relationships needed to determine K_{Ic} from the arrest length a_c, using both approximate analytical equations in Section 2 and accurate finite element

(FE) simulations in Section 3. Then, in Section 4, the implementation of the idea with respect to the real cracking process is explained. A proof of concept dealing with the determination of the fracture toughness of ~50 and ~100 nm-thick SiN films is provided in Section 5 before discussing the limitations and possible improvements of the technique in the conclusions.

2. Test configurations and analytical solutions

2.1 General test configuration

The symmetric and asymmetric configurations proposed to implement the on chip crack testing method are shown in Fig. 2a with the definition of the parameters. All materials under interest are assumed to have a linear isotropic elastic behavior. The two actuator beams have a length L_a, width W_a (or $2W_a$ for the symmetric design), thickness t_a, internal stress σ_a^{int}, Young's modulus E_a and Poisson ratio ν_a. The test specimen has a length L, width W ($2W$ for the symmetric design), thickness t, internal stress σ^{int}, Young's modulus E, Poisson ratio ν, and involves a crack of length a ($2a$ for the symmetric design). Upon release from the substrate, each actuator contracts with a displacement u and the specimen thus extends by $2u$. The displacement is determined by imposing force equilibrium between the two components of the structure. In order to treat the problem analytically, one thus assumes that the displacement field applied to the specimen along the connection line is not significantly varying over the width W_a, see Fig. 2b. This assumption will be assessed in section 3.

The problem can be decomposed in two parts, see Fig. 2c:

a) On the actuator side, the total strain ε_a is the sum of the elastic strain ε_a^{el} and of the mismatch strain ε_a^{mis}

$$\varepsilon_a = \varepsilon_a^{el} + \varepsilon_a^{mis}, \tag{2}$$

which leads to

$$-\frac{u}{L} = \frac{\sigma_a}{E_a} - \frac{\sigma_a^{\text{int}}}{E_a}\left(1-\nu_a\right), \tag{3}$$

where the minus sign on the left hand side comes from that u is defined positive when the actuator contracts and the $\left(1-\nu_a\right)$ term is due to initially equibiaxial internal stress. One can isolate the displacement produced by each actuator as

$$u = \frac{L_a}{E_a}\left(\sigma_a^{\text{int}}\left(1-\nu_a\right)-\sigma_a\right) = \frac{L_a}{E_a}\left(\sigma_a^{\text{int}}\left(1-\nu_a\right)-\frac{F}{t_a\beta W_a}\right), \tag{4}$$

where $\beta = 1$ or 2 whether the asymmetric or symmetric configurations are respectively considered.

b) On the specimen side, the total displacement that is applied, $2u$, is related to the corresponding force through the compliance function of the specimen C, when neglecting any internal stress σ^{int} in the specimen, as

$$\frac{2u}{F} = C\left(E, a, W_a, W, L\right) = \frac{1}{E} C^*\left(a, \frac{W_a}{W}, \frac{L}{W}\right). \tag{5}$$

The force F is obtained by combining (4) and (5):

$$F = \left[\frac{\left(1-\nu_a\right) L_a}{\dfrac{L_a}{t_a \beta W_a} + \dfrac{E_a}{E} \dfrac{C^*\left(a, \dfrac{W_a}{W}, \dfrac{L}{W}\right)}{2}} \right] \sigma_a^{\text{int}}. \tag{6}$$

The generic expression for the stress intensity factor K_I is given by

$$K_I = \frac{F}{\beta t W^*} Y\left(\frac{a}{W}, \frac{W_a}{W}, \frac{L}{W}\right) f\left(a\right) = \left(1-\nu_a\right) \sigma_a^{\text{int}} \sqrt{L_a}\, Y \frac{f\left(a\right)}{\sqrt{W}} \frac{\dfrac{t_a W_a}{t W^*} \sqrt{\dfrac{W}{L_a}}}{1 + \dfrac{E_a}{E} \dfrac{C^* t_a \beta W_a}{2 L_a}} \tag{7}$$

where W^* is an effective width which varies between W_a and W depending on the exact geometry, see further. Equation 7 shows that K_I is, as expected, proportional to σ_a^{int}.

Four fracture mechanics geometries shown in Figure 3 constitute known limit configurations for the general test structures shown in Fig. 2:

- (asymmetric) If $W_a = W$, the specimen geometry corresponds to a Single Edge Notched Tension (SENT) geometry;
- (symmetric) If $W_a = W$, the specimen geometry corresponds to a Centre Cracked Panel (CCP) geometry;
- (asymmetric) If $W \gg L$, the specimen geometry corresponds to a Double Cantilever Beam (DCB1) geometry;
- (symmetric) If $W \gg L$, the specimen geometry corresponds to a "double" Double Cantilever Beam (DCB2) geometry.

These limit configurations will be discussed in more details in the next subsections.

2.2 SENT and CCP

The SENT and CCP geometries are widely used in fracture mechanics and accurate solutions for K_I are available when expressed under the following form

$$K_I = \frac{F}{\beta W t} Y\left(\frac{a}{W}\right)\sqrt{\pi a}\,, \tag{8}$$

with $W \equiv W_a$. Several authors worked out accurate solutions for the SENT geometry (e.g. Brown and Srawley, 1966, Tada, 2000) such as

$$Y_{SENT}\left(\frac{a}{W}\right) = 1.122 - 0.231\left(\frac{a}{W}\right) + 10.55\left(\frac{a}{W}\right)^2 - 21.71\left(\frac{a}{W}\right)^3 + 30.382\left(\frac{a}{W}\right)^4 \text{ (for } \frac{a}{W} \le 0.6\text{)}, \tag{9}$$

hence, $$Y_{SENTapprox}\left(\frac{a}{W}\right) = 1.122 \text{ for small } a. \tag{10}$$

The corresponding function for the CCP geometry has been proposed by Irwin (1957) as

$$Y_{CCP}\left(\frac{a}{W}\right) = 1 + 0.128\left(\frac{a}{W}\right) - 0.288\left(\frac{a}{W}\right)^2 + 1.525\left(\frac{a}{W}\right)^3\,, \tag{11}$$

hence, $$Y_{CCPapprox}\left(\frac{a}{W}\right) = 1 \text{ for small } a. \tag{12}$$

The compliance function C can be determined using the classical fracture mechanics relationships (in mode I):

$$G = \frac{F^2 \partial C}{2t\partial a}, \tag{13}$$

and

$$G = \frac{K_I^2}{E^*}, \tag{14}$$

with $E^* = E/\left(1-\nu^2\right)$ in plane strain and $E^* = E$ in plane stress. Hence, one can obtain the compliance C by integration of

$$\frac{\partial C}{\partial a} = \frac{2}{E^* \beta^2 W^2 t}\left\{Y\left(\frac{a}{W}\right)\right\}^2 \pi a\,, \tag{15}$$

leading, for small a (i.e. $Y = 1.12$ or 1 for SENT and CCP, respectively), to

$$C_{SENT\,approx} = \frac{1}{EtW}\left[\frac{1.12^2 \pi \alpha_2 a^2}{W} + \alpha_3 L\right], \tag{16}$$

$$C_{CCP\,approx} = \frac{1}{2EtW}\left[\frac{\pi \alpha_2 a^2}{2W} + \alpha_3 L\right], \tag{17}$$

with $\alpha_2 = 1-\nu^2$ in plane strain and $\alpha_2 = 1$ in plane stress, and $\alpha_3 = 1-\nu^2$ when the specimen is attached at its upper and lower edges and $\alpha_3 = 1$ when the specimen is free at the edges. The more exact expressions of the C's are of limited interest in the present context. The final expression for K_I is given by

$$K_{I\ SENTapprox} = \left(1-\nu_a\right)\sigma_a^{\text{int}}\sqrt{L_a}\,\frac{1.12\sqrt{\pi\frac{a}{W}}\sqrt{\frac{W}{L}}\sqrt{\frac{L_a}{L}}}{\frac{L_a}{L}\frac{t}{t_a} + \frac{E_a}{2E}\left(\alpha_2 1.12^2 \pi\left(\frac{a}{W}\right)^2\frac{W}{L} + \alpha_3\right)}, \tag{18}$$

$$K_{I\ CCPapprox} = \left(1-\nu_a\right)\sigma_a^{\text{int}}\sqrt{L_a}\,\frac{\sqrt{\pi\frac{a}{W}}\sqrt{\frac{W}{L}}\sqrt{\frac{L_a}{L}}}{\frac{L_a}{L}\frac{t}{t_a} + \frac{E_a}{2E}\left(\alpha_2 \frac{\pi}{2}\left(\frac{a}{W}\right)^2\frac{W}{L} + \alpha_3\right)}, \tag{19}$$

valid at small crack length. In the limit where the crack length tends to zero, these expressions become

$$K_{I\ SENT\ \text{or}\ CCP\ a\to 0} = \left(1-\nu_a\right)\sigma_a^{\text{int}}\sqrt{L_a}\,\frac{Y\sqrt{\pi\frac{a}{W}}\sqrt{\frac{W}{L}}\sqrt{\frac{L_a}{L}}}{\frac{L_a}{L}\frac{t}{t_a} + \frac{E_a}{2E}\alpha_3}\ . \tag{20}$$

The stress intensity factor K_I can thus be normalized by $\left(1-\nu_a\right)\sigma_a^{\text{int}}\sqrt{L_a}$ and depends on 6 non dimensional parameters: a/W, t/t_a, L_a/L, L/W, E/E_a, and ν_a.

If the specimen is much more compliant than the actuator and/or the actuator is very short, then the stress intensity factor for very small crack lengths is approximated by

$$K_{I\ SENT,CCP}\left(E \ll E_a\right) = \left(1-\nu_a\right)\sigma_a^{\text{int}}\sqrt{L_a}\,\frac{2E}{\alpha_3 E_a}Y\sqrt{\pi\frac{a}{W}}\sqrt{\frac{W}{L}}\sqrt{\frac{L_a}{L}}\ . \tag{21}$$

while if the specimen is much stiffer than the actuator and/or if the actuator is very long, the relationship becomes

$$K_{I\ SENT,CCP}\left(E \gg E_a\right) = \left(1-\nu_a\right)\sigma_a^{\text{int}}\sqrt{L_a}Y\sqrt{\pi\frac{a}{W}}\sqrt{\frac{W}{L}}\sqrt{\frac{L}{L_a}}\frac{t_a}{t}, \tag{22}$$

showing no effect of E/E_a . Indeed, if the specimen is very stiff (i.e. small crack length and high Young's modulus), the actuator remains, after release, almost fully loaded and the applied stress is close to the internal stress σ_a^{int}, independently of the actuator length.

These two geometries are adapted to represent the test configurations of Fig. 2 if $L \gg W$ (whatever the ratio W/W_a) or if $W \approx W_a$ (whatever the ratio L/W). Figure 4 shows the variation of $K_I/\left(1-\nu_a\right)\sigma_a^{\text{int}}\sqrt{L_a}$ as a function of a/W in a SENT geometry for

(a) different E/E_a , with $L/W=3$, $W/W_a=1.5$, $L_a/L=1$ or 5, $t/t_a=1$, $\nu_a=0.3$;
(b) different W/W_a (but still not too different than 1 otherwise the use of the CCP or SENT configuration is not appropriate anymore), $E/E_a=1$, $L/W=3$, $L_a/L=5$, $t/t_a=1$, $\nu_a=0.3$;
(c) different L/W , $E/E_a=1$, $W/W_a=1.5$, $L_a/L=5$, $t/t_a=1$, $\nu_a=0.3$.

Fig. 4a shows that the effect of E_a/E can be neglected as long as the actuator is long enough. This is important to allow the determination of the fracture toughness of a material film without knowing its Young's modulus. If the actuator is short, then a very stiff specimen prevents the actuator to contract and lead to larger forces and thus larger K_I. The results of Fig. 4b and 4c must be considered with care. When W becomes significantly different than W_a and L is not much larger than W, then the factors W/W_a and L/W will start playing a role and the function Y of equation (7) cannot be assimilated anymore to the SENT and CCP solutions. These effects can only be captured using the FE simulations of the next section.

When the specimen involves an internal stress σ^{int}, no analytical expression can be found for K_I in the general case. However, approximate solutions can be easily determined for very small crack length a. In the case of the CCP configuration, the expressions are different whether the specimen is clamped at its end or not. Indeed, if the specimen is clamped, the transverse internal stress will not relax. The expression of K_I is given by

$$K_{I\ CCP\ a\to 0\ clamped} = 2Y\sqrt{L_a}\sqrt{\frac{\pi a}{W}}\sqrt{\frac{W}{L}}\sqrt{\frac{L_a}{L}}\left(\frac{\left(1-\nu_a\right)\sigma_a^{\text{int}}+\frac{E_aL}{2EL_a}\left(1-\nu^2\right)\sigma^{\text{int}}}{\frac{E_a\left(1-\nu^2\right)}{E}+\frac{2tL_a}{t_aL}}\right), \tag{23}$$

$$K_{I\ CCP\ a\to 0\ not\ clamped} = 2Y\sqrt{L_a}\sqrt{\frac{\pi a}{W}}\sqrt{\frac{W}{L}}\sqrt{\frac{L_a}{L}}\left(\frac{\left(1-\nu_a\right)\sigma_a^{\text{int}} + \frac{E_a L}{2EL_a}\left(1-\nu\right)\sigma^{\text{int}}}{\frac{E_a}{E}+\frac{2t}{t_a}}\right). \qquad (24)$$

These solutions show that when the test specimen involves significant internal stress, the normalization of K_I is complicated. In addition, the case of the SENT specimen is more complex than the CCP geometry because the specimen is always free along the cracked edge. The presence of internal stress in a SENT specimen will lead to a bending component in the actuator arms that is difficult to model analytically in the general case (except if the actuator arms are very long). The displacement field at the specimen edges shown in Fig. 2b are less and less homogenous as well. Aside from bending, twisting of the specimen and of the actuator can be expected, see Section 5. Finally, note that the presence of the transverse internal stress can favour crack kinking.

2.3 DCB geometry

At the other extreme, when W is much larger than W_a and L significantly smaller than W, the DCB geometry shown in Fig. 3c, widely used in composite and adhesive bond testing (Blackman and Kinloch, 2001, Robinson et al., 2004), constitutes the reference limit geometry. The expression of the energy release rate valid for sufficiently long beams is written as

$$G_{DCB\ asym} = 2\times\frac{F^2}{2t}\frac{\partial C_{half\ DCB\ asym}}{\partial a}, \qquad (25)$$

$$G_{DCB\ sym} = 4\times\frac{F^2}{8t}\frac{\partial C_{quarter\ DCB\ sym}}{\partial a}, \qquad (26)$$

with

$$C_{half\ DCB\ asym} = \frac{u}{F} = \frac{a^3}{3EI} = \frac{32a^3}{EtL^3}, \qquad (27)$$

$$C_{quarter\ DCB\ sym} = \frac{u}{F/2} = \frac{a^3}{6EI} = \frac{16a^3}{EtL^3}, \qquad (28)$$

where I is the second moment of inertia. The final expressions for the energy release rates are

$$G_{DCB\ asym} = \frac{96F^2a^2}{Et^2L^3}, \qquad (29)$$

$$G_{DCB\,sym} = \frac{24F^2a^2}{Et^2L^3}. \tag{30}$$

Note that more accurate expressions can be determined accounting for elastic foundation and shear effects (see e.g. Li et al., 2004). Using eqn (14), some elementary manipulations lead to

$$K_{I\ DCB\,asym} = \left(1-\nu_a\right)\sigma_a^{\text{int}}\sqrt{L_a}\,\frac{4\sqrt{\frac{6L_a}{\alpha_2 L}}}{32\frac{E_a}{E}\frac{a^2}{L^2}+\frac{L}{a}\frac{L_a}{W_a}\frac{t}{t_a}}\ , \tag{31}$$

$$K_{I\ DCB\,sym} = \left(1-\nu_a\right)\sigma_a^{\text{int}}\sqrt{L_a}\,\frac{4\sqrt{\frac{6L_a}{\alpha_2 L}}}{16\frac{E_a}{E}\frac{a^2}{L^2}+\frac{L}{a}\frac{L_a}{W_a}\frac{t}{t_a}}\ , \tag{32}$$

Same as for the CCP and SENT configurations, K_I can be normalized by $\left(1-\nu_a\right)\sigma_a^{\text{int}}\sqrt{L_a}$. Figure 5 shows the variation of $K_I/\left(1-\nu_a\right)\sigma_a^{\text{int}}\sqrt{L_a}$ as a function of *a/W* for

(a) different E/E_a with L/W=0.1, W/W_a = 10, L_a/L = 5, t/t_a = 1, ν_a = 0.3
(b) different L/W with E/E_a = 1, W/W_a = 10, L_a/L = 5, t/t_a = 1, ν_a = 0.3
(c) different W_a/W with E/E_a = 1, W/W_a = 10, L_a/L = 5, t/t_a = 1, ν_a = 0.3

For all these dimensions, K_I decreases with *a/W*. Fig. 5a shows that for long enough actuators and small *L/W*, the ratio E/E_a has a very limited effect on K_I especially for high *a*/*W* values. Fig. 5b confirms that the effect of *L/W* for high W/W_a values can be neglected when the specimen length *L* becomes significantly larger than *W* especially if there is no significant difference between *E* and E_a. For the DCB configuration, W/W_a has no impact on the K_I value.

The analysis performed in this section provides first insights about the variations of K_I, while revealing the important non-dimensional parameters and proper normalization. The stress intensity factor K_I increases with crack length at small *a/W* and decreases with crack length at large *a/W*. This will have consequences on the stability of the fracture process as discussed later in Section 4.

3. Finite element simulations

Full finite element (FE) simulations have been performed with the software Abaqus to determine the relationship between the stress intensity factor K_I and the crack length *a* for the entire range of dimensions of interest, particularly for intermediate values of W/W_a, i.e. when

the analytical solutions of Section 2 cannot be applied. The mechanical behavior of both specimen and actuator materials follows linear isotropic elastic Hooke's law. Realistic ranges of parameters are dictated by the fabrication process (see Section 5) and lead to

a/W: entire range from almost 0 to almost 1;
L/W: from 0.05 to 1;
W/W_a: from 1 (though not realistic) to 10;
t/t_a: 1 (only one value is needed as it will play the same role as changing the value of σ_a^{int});
E/E_a : 0.1 to 10;
L_a/L :1 to 100;
$\nu = 0.3$;
$\nu_a = 0.3$.

The FE mesh shown in Figure 6 consists of 4-node bilinear plane stress elements with reduced integration (CPS4R). The collapsed quadrilateral quarter element technique was used to capture the singularity field near the crack tip in order to extract accurate values of K_I. Each simulation consists of two steps:

In step 1, the entire test structure is attached to a rigid substrate. A fictitious thermal loading ΔT is applied in order to generate an equibiaxial internal stress field of magnitude

$$\sigma^{\text{int}} = \frac{E}{1-\nu}\alpha\Delta T\,. \tag{33}$$

Hence, different stress levels can be induced in both the test and actuator materials by varying the fictitious thermal expansion exponent α or by imposing different ΔT in the two materials.

In step 2, the entire test structure is released from the substrate by suppressing the boundary conditions at each node of the bottom part of the model. Only the nodes at the extremities of the actuators remain clamped in the three directions of space, as well as the extremities of the test specimen in the case of a clamped specimen. As the materials are both linear elastic, the sequencing and the dynamics of the release process do not matter. This was verified for sanity check by imposing different release sequences. This would not be true in the case of plastically deforming materials for which the exact history of the release process would be important. During this step, the actuator beams contract and the test specimen elongates to reach force equilibrium. Careful convergence analysis has been performed to ensure that the results were independent of the level of mesh refinement.

Figure 7 shows the variations of the normalized stress intensity factor $K_I \big/ \left(1-\nu_a\right)\sigma_a^{\text{int}}\sqrt{L_a}$ for different levels of internal stress for both symmetric and asymmetric test geometries with

no internal stress in the test specimen. The linearity between K_I and internal stress is perfectly respected, as expected. At first, K_I increases linearly with crack length a as anticipated based on the SENT and CCP solutions (see Section 2), reaches a maximum and then decreases as $1/a^2$ in agreement with the DCB solution (see Section 2).

Figure 8 shows the variation of the normalized stress intensity factor with a/W for different L_a/L ratio, for (a) the symmetric and (b) asymmetric configurations, and for three different specimen stiffnesses, $E_a/E = 1$ (continuous line), $E_a/E = 10$ (dotted lines) and $E_a/E = 0.1$ (dashed lines). The specimen length has an impact on the magnitude of K_I mainly in the symmetric configuration. Furthermore, the effect of specimen length is opposite whether small or long crack lengths are considered. The elastic mismatch ratio E_a/E significantly affects K_I. Stiff actuators lead to smaller K_I, with all other parameters being fixed. The reason is that a stiff actuator, for a given internal stress σ_a^{int}, corresponds to a small mismatch strain, thus to a small contraction potential and to small imposed displacement to the test specimen.

Figure 9 exhibits the variations with a crack length of the normalized K_I in the asymmetric configuration for different width ratios W_a/W and for (a) a small L_a/L ratio and (b) for a high L_a/L ratio. K_I is independent of W_a/W for small crack lengths only. This shows the limited validity of the analytical solution of Section 2 for intermediate crack lengths (i.e. $a/W > 0.1$) when W_a is different than W.

Figure 10 shows the effect of the presence of internal stress in the test material (as will be the case in the experimental proof of concept of Section 5). The internal stress in the test material is taken equal to the one of the actuator material. This allows covering the interesting case of a single material pulling on itself, i.e. when the actuator and the specimen are deposited simultaneously. This case is considered as an upper bound for the effect of specimen internal stress, as the actuator material is indeed chosen for its high internal stress level implying that the specimen internal stress is then large as well. As already shown by the analytical equations (23) and (24), a tensile internal stress in the specimen can significantly contribute to raising the stress intensity factor. The effect of the internal stress of the specimen is more pronounced for short actuators and disappears for long actuators. The effect is also more pronounced for large E_a/E ratio. The effect is smaller for the asymmetric configuration as the internal stress is partly relaxed due to the free edge. A final point of discussion concerns the possible effect of the so-called T stress that develops in the symmetric configuration when clamped, which is the case for all the data reported in this section. The T stress is the constant stress directed parallel to the crack tip in the K-field solution that affects the stress state in the fracture process zone. The presence of a T stress can potentially affect the fracture toughness of the material by modifying the hydrostatic stress at the crack tip. It can also strongly affect the crack kinking behaviour.

More comprehensive parameter variations have been performed to allow covering the entire range of parameters of interest. These are not presented here as they do not reveal any particular relationships or trends out of the one presented above.

4. Cracking process

As a transition towards the experimental assessment of the on-chip fracture test methodology, the phenomenology of the cracking process is now addressed based on the variations of K_I predicted in sections 2 and 3. As a matter of fact, the main purpose of the analysis performed in sections 2 and 3 was to extract the value of K_I as a function of crack length, which, in real tests, will be the final crack length. But, in a real cracking process, there are at least five additional elements that must be taken into account: (i) the cracking process starts from a blunt notch and not from a sharp pre-crack, (ii) the release of the actuator is progressive owing to a small tapering over its length (see Fig. 1); (iii) the variation of K_I with crack length can lead to an unstable cracking process before arrest; (iv) subcritical crack growth can occur with time after full release; (v) a R curve effect is possible, meaning a variation of K_{Ic} with crack growth.

Figure 11 shows the typical variation of the K_{Ic}^*, the value of K_I at cracking initiation, as a function of the initial crack tip opening. Above a threshold value, which roughly corresponds to the critical crack tip opening displacement, K_{Ic}^* increases with the initial crack opening due to the extra energy needed to generate a sharp crack in the zone in front of the notch. In other words, in the real test configuration, the crack will initiate at a value of K_I larger than K_{Ic}.

The cracking process can be schematically analysed based on Figure 12 for a test structure with an initial notch length a_0. The notch radius δ_0 implies a pseudo fracture toughness K_{Ic}^* which is higher than K_{Ic}. Fig. 12a represents the schematic evolution of the K_I versus crack length relationship as the actuator is released. The different curves correspond to different instants of the progressive release process (the tapered shape of the actuator ensure, in the real experimental application a progressive release, see Fig. 1). In addition, the test specimens are designed narrower than the minimum width of the actuator to allow their full release before the actuator starts pulling on it. Different instants of the release thus mean different effective lengths of the actuator L_a. At the early stages of the release, L_a is small and K_I increases with increasing L_a as revealed in Sections 2 and 3. Even after full release of the test structure, the magnitude of K_I for a_0 in Fig. 12a is not such sufficient to allow cracking initiation from the notch root. Fig. 12b shows that for a longer actuator cracking initiates at the notch root when $K_I = K_{Ic}^*$ before full release. The crack then propagates in an unstable manner; see "(2)", until K_I decreases down to K_{Ic}, assuming no R-curve effect. This propagation is very fast and the release (which takes seconds or minutes, see Section 5) can be considered as frozen during that time. Then, a stable crack propagation "(3)" process can still occur during the last phase of the release of the actuator. Finally, ageing or rate dependent effects can lead to subcritical crack growth under decreasing K_I values as also depicted in Fig. 12b.

The process analysed based on Figure 12 indicates that working with small initial cracks a_0 will lead to long unstable crack propagation that is more difficult to control than if longer initial cracks are used. Long crack propagation is more prone to crack kinking. It also indicates the

importance to start with an initial notch opening that is as sharp as possible. A final aspect which can complicate the analysis is when the test material exhibits an R-curve effect. If the R-curve effect is small, associated to a small increase of K_{Ic} with crack growth propagation, one can look not only at the final crack length but also at the crack advance Δa from initiation to arrest. Indeed, depending on the initial notch length, there will be different crack advance before arrest. The variation of K_{Ic} with crack advance can thus be qualitatively obtained. In the case of large R-curve effect, the test material then involves significant dissipation at the crack tip and in the crack wake, meaning that the tearing resistance is high. This cannot be treated by linear elastic fracture mechanics due to large plastic zone size and an elastoplastic treatment, out of the scope of the present work, must be performed.

5. Experimental testing

This section describes first the generic fabrication steps of the on chip fracture test structures before proposing a specific process flow adapted to SiN actuators pulling on a cracked SiN specimen. Then, the different measurements required to determine K_{Ic} are explained. The different experimental problems that have been encountered are listed before presenting and discussing a series of successful results.

5.1 Generic fabrication process

The fabrication process relies on micro- and nano-fabrication techniques as used in microelectronic and MEMS technologies. It involves three different layers deposited on top of a bulk silicon substrate:

(i) The role of the "sacrificial layer" is to support the top layers during fabrication and to enable the release from the substrate. In many applications of the on chip technique, SiO_2 was used (Coulombier et al., 2010, Gravier et al., 2009). This layer can be etched using a HF-based solution. When possible, the silicon substrate can also play the role of a sacrificial layer (see Ghidelli et al, 2017), to be etched with TMAH solution or XeF_2, avoiding the need for deposition of an extra layer. The selection of the sacrificial layer and etchant depends on the actuator and test material, in order to have the highest etching selectivity.

(ii) The "actuator layer" is selected primarily based on the potential to exhibit large tensile internal stress upon deposition. The method requires the actuator to remain linear elastic, with no relaxation under stress. It should be highly reproducible to avoid batch-to-batch variations, and this even though the internal stress will be systematically measured using Stoney method (Stoney, 1909). The favorite actuator layer is made of Si_3N_4 deposited by LPCVD (Low Pressure Chemical Vapour Deposition).

(iii) The “specimen layer” is the layer of interest from which the fracture toughness must be extracted.

Both actuator and specimen layers can be patterned by optical or e-beam lithography as explained in earlier works, e.g. (Gravier et al., 2009, Vayrette et al., 2015). As explained in Section 4, the test structures are designed to allow the full release of the test specimen before the actuator. This is ensured when the length L of the test specimen is smaller than the width of the actuator W_a or 2 W_a. A tapered shape is imposed to the actuators in order to enforce a progressive release and loading process. This also means that the correspondence with the mechanical analysis of Sections 2 and 3 must be made for the proper average actuator width.

5.2 Specific process for SiN pulling on SiN

For the specific case of test specimens having sufficiently high tensile internal stress, the fabrication can be simplified to only one film deposition, hence one lithography step. Furthermore, the pattern of the actuator and specimen layer can be merged into one design. This also avoids alignment problems occurring sometimes when several lithography steps are performed. This is why this option has been preferred for a first validation of the method and to guide the fine tuning of the test design. LPCVD Si_3N_4 deposited at 790°C in a KOYO vertical furnace VF-1000 from Koyo Thermo Systems Company has been selected because it exhibits large internal stress, its properties are well known from prior works and it is also a material of interest in the field of MEMS and coatings. Here, Si_3N_4 films with thickness equal to 55 nm and 93 nm have been tested.

Patterning of the test structures is performed here by e-beam lithography (FEI XL30) using PMMA as a resist and a CHF_3/O_2 plasma for etching (Reactive Ion Etching). The e-beam technique was chosen because it is maskless which enables changing the parameters of the design easily from one batch to the next, hence accelerating the design evolution. Another advantage lies in the higher resolution that can be reached compared with optical lithography.

As explained in Section 4, the initial notch should be as sharp as possible to avoid excessive overload to induce cracking initiation. The resolution of the resist (PMMA) and the parameters of the e-beam lithography limit the minimum notch radius to ~ 0.3 μm showing again the importance of looking at a crack arrest test configuration.

After patterning of the Si_3N_4 layer, the last step of the process consists in releasing the test structures (actuators and specimen) by etching away the underneath silicon substrate. For this purpose XeF_2 was selected, allowing isotropic etching of silicon with high selectivity. The isotropy of the etching favours also the progressive release of the actuator. The etching is performed by pulses where XeF_2 is accumulated in an expansion chamber then injected in the etching chamber before being pumped out. Short pulses have been used to ensure a high

selectivity between the silicon from the sacrificial layer and the Si_3N_4 from the actuator layer (Poncelet et al., 2018).

5.3 Metrology and design rules

Extraction of the fracture toughness of the specimen material requires the measurements of the material and geometrical parameters affecting K_I, i.e. $(1-\nu_a)\sigma_a^{\text{int}}\sqrt{L_a}$, a/W , t/t_a , L_a/L , L/W , W_a/W and ν_a. The parameter E/E_a plays no role here as the specimen and actuators are made of the same material. If needed, the Young's modulus of the actuator and specimen materials can be determined by combining nanoindentation results (but with an accuracy that deteriorates as the thickness gets smaller and smaller) and the measurements of both internal stress and mismatch strain data using Stoney method (see next) and different test structures patterned on the same wafer, i.e. clamped-clamped beams or rotating sensors, see Gallacher et al. (2008) and Boé et al. (2009). One can also use the same concept of internal stress actuated structure to extract elastic properties of thin film materials, e.g. Gravier et al. (2009), Bhaskar et al. 2012, Pardoen et al. (2016).

The internal stress σ_a^{int} is measured by wafer curvature method relying on Stoney formula (Stoney, 1909):

$$\sigma_a^{\text{int}} = \sigma_f = \frac{E_s h_s^2}{6h_f(1-\nu_s)}\left(\frac{1}{R}-\frac{1}{R_0}\right), \tag{34}$$

where the subscripts *s* and *f* denote to the substrate and film, respectively, *h* is the thickness, *E* is the Young's modulus, *v* is Poisson ratio, and *R* is the radius of curvature of the substrate after deposition while R_0 is the radius before deposition. The value $\sigma_a^{\text{int}} = 1.11 \pm 0.05\,\text{GPa}$ was measured for the material tested in this study.

The Poisson ratio of SiN is taken from the literature as equal to $\nu_a = 0.28 \pm 0.05$ (Vlassak and Nix, 1992).

The thickness of the specimen (the same for actuator) is measured by ellipsometry using Cauchy models, $t = t_a = 55\,\text{nm}$ and $t = t_a = 93\,\text{nm}$, with an error of $\pm 1\,\text{nm}$.

All lengths and widths are measured after release of the test structures by SEM in order to take into account any lithography errors. The release is performed on a portion of the Si wafer involving typically 45 test structures produced by either e-beam lithography or photolithography. The test structures are inspected in a SEM in order to find samples in which a crack has been initiated and arrested inside the test specimen. Each test structure has a reference number. The crack length is measured as accurately as possible based on the length projected on the long axis of the specimen.

5.4 Experimental problems

Many attempts have been made on the SiN test structures to optimize the design guided by the theoretical analysis as well as by practical issues. The notch length a_0 was systematically varied between 0 and 28 μm and the actuator length L_a between 10 and 360 μm, while different actuator widths W_a and specimen lengths L were also tested.

Figure 13 shows a set of different released test structures. Fig. 13a is an example of a long notch in an asymmetric structure showing no crack initiation. Actually, the notch tip produced by e-beam was too coarse. This has been optimized in later attempts. Furthermore, the test structures are not perfectly plane, exhibiting some bending.

Fig. 13b shows an asymmetric design with the specimen is not clamped at the edge. A crack has been properly initiated, but the specimen undergoes significant out of plane distortion leading to a mode III component. Fig. 13c shows an example of a crack kinking out of the specimen and not allowing any measurements of K_{Ic} (except for an upper bound value). Fig. 13d shows an example of a specimen sticking on the substrate which possibly affects the cracking process as well. As a matter of fact, the asymmetric structures, especially when not clamped at the end, are often prone to crack kinking, stiction and out of plane distortion. This favours the systematic use of symmetric structures. Still, crack kinking out of the specimen are also observed for the symmetric test structures. Fig. 13f shows a problem that is common to all test structures, i.e. the underetching of all the edges of the test structures. This underetching will be always present and its influence cannot be neglected especially in small actuators lengths case. It should be measured and accounted for in the modelling of the test structures. In order to avoid this difficulty, allow comparison with the FE results of Section 3 and get as accurate results as possible, the actuators were only partially released. Further simulations similar to the one of Section 3, but with underetching, will be performed as one of the perspective of this work to properly account for this effect.

5.5 Proof of concept

Figure 14 shows a few examples of successful tests with a crack arresting inside the specimen with limited out of plane specimen bending. As mentioned in the previous section, the release was stopped before full completion to avoid the problem of underetching. Table 1 lists the characteristics of a series of successful test structures present on the same wafer (for a given thickness), three for t = 55 nm and twelve for t = 93 nm. These correspond all to asymmetric test configurations with the same notch radius and length. L_a^* is the released actuator length measured based on the last unreleased point of the actuator and W_a^* corresponds to the mean width of the released part of the actuator. As a matter of fact, a partially released actuator has not a straight rectangular release front but, instead, a triangular shape, which means that the

sides are already released while the center of the beam is still attached to the substrate. A few additional FE simulations have been performed with the more exact release profile to check whether this could significantly affect the results. For the characteristic dimensions of the present test structures, the effect was found to be less than 5%.

The extracted values of the fracture toughness K_{Ic} are given in the last column of Table 1, varying between 1.2 and 3.4 $\mathrm{MPa}\sqrt{\mathrm{m}}$, with a mean value equal to 2.0 $\mathrm{MPa}\sqrt{\mathrm{m}}$. Even though the lowest thickness seems to exhibit a lower fracture toughness, the number of results is not statistically sufficient to support this claim. The uncertainty on the extracted K_{Ic} mainly comes from the uncertainty on the actuator length measurement due to the problem of partial release which introduces visual inaccuracy in the determination of the length. One should also note that the uncertainty on the internal stress value, which is about 5% and on the factor $(1-\nu_a)$ which is about 10% leads to a possible systematic error of about 15% on the magnitude of K_{Ic}. More data would be needed to perform a sound Weibull type statistical analysis.

The mean K_{Ic} found in this study is close to the $1.8\,\mathrm{MPa}\sqrt{\mathrm{m}}$ obtained by Kim et al. (2016) on 250 nm thick plasma enhanced chemical vapour deposition (PEVCD) SiN using a test method where the film is deposited and tested on a polymer (PET) substrate. It is important to note that this value reported by Kim et al. (2016) required detailed non-linear FE analysis to correct for the effect of viscoplastic yielding of the substrate. This correction amounts to more than 25% compared with a purely elastic solution, showing the interest of a freestanding test configuration. Merle and Göken (2011), for LPCVD SiN films with thickness in the range 40 to 100 nm found a significantly larger mean K_{Ic} equal to $6.3\pm0.4\ \mathrm{MPa}\sqrt{\mathrm{m}}$ but based on a starter notch opening equal to ~250 nm possibly leading to an overestimation of the fracture toughness as explained with Fig. 11.

6. Conclusion and perspectives

A new concept of on-chip fracture mechanics test for thin freestanding films has been proposed, developed and applied to submicron SiN layers. The idea is to rely on a crack arrest measurement instead of a precracking initiation method to overcome the complication of generating atomically sharp precracks in micro-specimens. The actuation comes from internally stressed beams that, upon release, act as springs to load the crack specimen. The main contributions of this work are the following:

1. The new test method itself brings some fundamentally new capabilities compared to the current state of the art with, in principle, no limit on the lowest possible thickness that can be addressed, no need for precracking and the generation of vast amount of data once a viable process is found.

2. A theoretical analysis and application of existing reference fracture mechanics geometries to the present internal stress driven loading configuration reveal the key parameters affecting the magnitude of the stress intensity factor as function of crack length. Among others, the stress intensity factor scales linearly with the internal stress in the actuator.
3. An extensive set of FE simulations provides, for a wide range of parameter variations, the variation of the stress intensity factor with crack length. These results give the data to back out, from a crack length measurement, the corresponding (arrest) fracture toughness. The variation of K_I with crack length also provides important information regarding the cracking process, which involves an unstable propagation followed by stable cracking.
4. A proof of concept has been worked out. The test specimens have been successfully produced by a sequence of deposition, lithography and etching. The tests on 55 and 93 nm thick SiN films give a mean value of fracture toughness equal to $2.0\,\mathrm{MPa}\sqrt{\mathrm{m}}$.

This first proof of concept demonstrates the potential of the method. Still, the test geometries must be optimized to guarantee the maximum possible success rate along the following lines: (i) the main difficulty is to avoid the crack to deviate from mode I and to remain inside the test beam; one option is to work with tapered specimens, which requires additional efforts in terms of FE simulations to estimate the value of K_I; (ii) to avoid warping and out of plane effects which is improved by using a symmetric configuration; (iii) to make the initial notch as sharp as possible by optimizing the e-beam lithography; (iv) to avoid the underetching by specific chemical treatment of the substrate at the frontier of the test structure regions (or to model the underetching in the FE model). Note that other crack configurations are possible to induce mixed modes with inclined precracks for instance.

A key question is about the meaning of the arrest fracture toughness compared to the initiation toughness. If, for brittle materials with limited dissipation mechanisms, the arrest toughness is probably very close to the initiation toughness, this might not be true in more ductile films. This aspect requires further investigation as well as, for the later case, the extension to an elastoplastic fracture mechanics framework.

Aside from the determination of the fracture toughness of thin film materials, the method is particularly adapted to subcritical crack growth analysis. Similar to our earlier studies regarding creep in thin freestanding films, it is straightforward to monitor the evolution of crack length with time, hence of the corresponding stress intensity factor. The on chip test structures can be left in a controlled environment, either gas or temperature conditions, to address various kinds of ageing phenomena without monopolizing any test equipment. In particular, the test structures can also be used to look at crack growth under irradiation following the spirit of the work done on irradiation creep (Lapouge et al., 2016, 2017). Finally, the test structures can be characterized by TEM through etching the substrate underneath the test structure as in (Colla et al., 2015), possibly allowing in situ monitoring of the sub-critical crack growth mechanisms.

Acknowledgements

T.P. acknowledges the numerous scientific and non-scientific interactions with Norman Fleck over the last two decades, a unique blend of incisive thinking, rigour and humour. The authors are also very grateful to the staff of the WINFAB cleanroom facilities for the support in the experimental part of the research. The financial support of the UCL and Communauté Française through the ARC project "Naturist" are gratefully acknowledged.

References

Ballarini, R., Mullen, R. L., Yin, Y., Kahn, H., Stemmer, S., Heuer, A. H., 1997. The fracture toughness of polysilicon microdevices: a first report. Journal of Materials Research 12, 915-922.

Bellante, J.J., Kahn, H., Ballarini, R., Zorman, C., Mehregany, M., Heuer, A.H., 2005. Fracture Toughness of Polycrystalline Silicon Carbide Thin Films. Applied Physics Letters, 86, 071920 - 071920.

Beuth Jr, J. L., 1992. Cracking of thin bonded films in residual tension. International Journal of Solids and Structures 29, 1657-1675.

Bhaskar, U., Passi, V., Houri, S., Escobedo-Cousin, E., H. Olsen, S., Pardoen, T., Raskin, J.P., 2012. On-chip tensile testing of nanoscale silicon free-standing beams. Journal of Materials Research 27, 571-579.

Blackman, B., Kinloch, A., 2001. Fracture tests on structural adhesive joints. European Structural Integrity Society 28, 225-267.

Boe, A., Safi, A., Coulombier, M., Pardoen, T., Raskin, J. P., 2009. Internal stress relaxation based method for elastic stiffness characterization of very thin films. Thin Solid Films, 518, 260-264.

Brown, W.F., Srawley, J.E., 1966. Plane Strain Crack Toughness Testing of High-Strength Metallic Materials. ASTM STP. 410. American Society for Materials and Testing, USA.

Chasiotis, I., Cho, S. W., Jonnalagadda, K., 2006. Fracture toughness and subcritical crack growth in polycrystalline silicon. Journal of Applied Mechanics 73, 714-722.

Chasiotis, I., Knauss, W. G., 2003a. The mechanical strength of polysilicon films: Part 1. The influence of fabrication governed surface conditions. Journal of the Mechanics and Physics of Solids 51, 1533-1550.

Chasiotis, I., & Knauss, W. G., 2003b. The mechanical strength of polysilicon films: Part 2. Size effects associated with elliptical and circular perforations. Journal of the Mechanics and Physics of Solids 51, 1551-1572.

Colla, M. S., Amin-Ahmadi, B., Idrissi, H., Malet, L., Godet, S., Raskin, J. P., ... & Pardoen, T., 2015. Dislocation-mediated relaxation in nanograined columnar palladium films revealed by on-chip time-resolved HRTEM testing. Nature communications, 6, 5922.

Coulombier, M., Boé, A., Brugger, C., Raskin, J.P., Pardoen, T., 2010. Imperfection-sensitive ductility of aluminium thin films. Scripta Materialia 62, 742-745.

Espinosa, H. D., Peng, B., 2005. A new methodology to investigate fracture toughness of freestanding MEMS and advanced materials in thin film form. Journal of microelectromechanical systems 14, 153-159.

Fabrègue, D., Andre, N., Coulombier, M., Raskin, J.P., 2007. Multipurpose nanomechanical laboratory: five thousands micromachines on a wafer. Micro and Nanoletters 2, 13-16

Gallacher, B.J., O'Neill, A.G., Bull, S., Wilson, C., & Horsfall, A.B., 2008. Analysis of a Passive Sensor for Predicting Process-Induced Stress in Advanced Integrated Circuit Interconnect. *IEEE Transactions on Device and Materials Reliability 8*, 174-181.

Ghidelli, M., Idrissi, H., Gravier, S., Blandin, J.J., Raskin, J.P., Schryvers, D., Pardoen T., 2017. Homogeneous flow and size dependent mechanical behaviour in highly ductile metallic glass films. Acta Materialia 131, 246-259.

Gravier, S., Coulombier, M., Safi, A., Andre, N., Boe, A., Raskin, J.P., Pardoen, T., 2009. New MEMS – Based micromechanical testing laboratory – Application to aluminium, polysilicon and silicon nitride. Journal of Microelectromechanical Systems 18, 555-565.

Hutchinson, J.W., Suo, Z., 1992. Mixed mode cracking in layered materials. Advances in Applied Mechanics 29, 63-191.

Iqbal, F., Ast, J., Göken, M., Durst, K., 2012. In situ micro-cantilever tests to study fracture properties of NiAl single crystals. Acta Materialia 60, 1193-1200.

Irwin, G.R., 1957. Analysis of stresses and strains near the end of a crack traversing a plate. J Appl Mech 24, 361–364.

Jiang, Z., Lu, F. X., Tang, W. Z., Wang, S. G., Tong, Y. M., Huang, T. B., Liu, J. M., 2000. Accurate measurement of fracture toughness of freestanding diamond films by three-point bending tests with sharp pre-cracked specimens. Diamond and related materials 9, 1734-1738.

Jonnalagadda, K., SW., Chasiotis, I., Friedmann, T., Sullivan, J., 2008. Effect of intrinsic stress gradient on the effective mode-I fracture toughness of amorphous diamond-like carbon films for MEMS. JMPS 56, 388-401.

Kahn, H., Ballarini, R., Mullen, R. L., Heuer, A. H., 1999. Electrostatically actuated failure of microfabricated polysilicon fracture mechanics specimens. In Proceedings of the royal society of London a: mathematical, physical and engineering sciences 455, 3807-3823.

Kahn, H., Tayebi, N., Ballarini, R., Mullen, R. L., Heuer, A. H., 2000. Fracture toughness of polysilicon MEMS devices. Sensors and Actuators A: Physical 82, 274-280.

Keller, C. G., 1998. Microfabricated silicon high aspect ratio flexures for in-plane motion. PhD dissertation, University of California, Berkeley, USA

Kim, K., Luo, H., Singh, A.K., Zhu, T., Graham, S., Pierron, ON., 2016. Environmentally assisted cracking in silicon nitride barrier films on poly(ethylene terephthalate) substrates. ACS Applied Materials & Interfaces 8, 27169-27178.

Lapouge, P., Onimus, F., Coulombier, M., Raskin, J.P., Pardoen, T., Bréchet, Y. 2017. Creep behavior of submicron copper films under irradiation, Acta Materialia 131, 77-87.

Lapouge, P., Onimus, F., Vayrette, R., Raskin, J. P., Pardoen, T., & Bréchet, Y. (2016). A novel on chip test method to characterize the creep behavior of metallic layers under heavy ion irradiation. Journal of Nuclear Materials, 476, 20-29.

Li, S., Wang, J.Z., Thouless, M.D., 2004. The effects of shear on delamination in layered materials. Journal of the Mechanics and Physics of Solids. 52. 193-214.

Li, X., Bhushan, B., 1998. Measurement of Fracture Toughness of Ultra-Thin Amorphous Carbon Films. Thin Solid Films 315, 214 – 221.

Massl, S., Thomma, W., Keckes, J., Pippan, R., 2009. Investigation of fracture properties of magnetron-sputtered TiN films by means of a FIB-based cantilever bending technique. Acta Materialia 57, 1768-1776.

Merle, B., Göken, M., 2011. Fracture toughness of silicon nitride thin films of different thicknesses as measured by bulge tests. Acta Materialia 59, 1772-1779.

Pardoen, T., Colla, M.S., Idrissi, H., Behnam, A.A., Wang, B., Schryvers, D., Bhaskar, U.K., Raskin, J.P., 2016. A versatile lab-on-chip test platform to characterize elementary deformation mechanisms and electromechanical couplings in nanoscopic objects. Comptes Rendus Physique 17, 485-495.

Poncelet, O., Rasson, J., Tuyaerts, R., Coulombier, M., Kotipalli, R., Raskin, J. P., Francis, L. A., 2018. Hemispherical cavities on silicon substrates: an overview of micro fabrication techniques. Materials Research Express 5, 045702.

Robinson, R., Das, S., 2004. Mode I DCB testing of composite laminates reinforced with z-direction pins: a simple model for the investigation of data reduction strategies. Engineering Fracture Mechanics 71, 345–364.

Sharpe, W. N., Yuan, B., & Edwards, R. L., 1997. Fracture tests of polysilicon film. MRS Online Proceedings Library Archive 505.

Stoney, G. G., 1909. The tension of metallic films deposited by electrolysis. Proc. R. Soc. Lond. A, 82, 172-175.

Tada, H., Paris, P.C., Irwin, G.R., 2000. The stress analysis of cracks handbook. ASME Press, New York, USA.

Tsuchiya, T., Sakata, J., & Taga, Y., 1997. Tensile strength and fracture toughness of surface micromachined polycrystalline silicon thin films prepared under various conditions. MRS Online Proceedings Library Archive 505.

Vayrette, R., Raskin, J.P., Pardoen, T., 2015. On-chip fracture testing of freestanding nanoscale materials. Engineering Fracture Mechanics 150, 222-238.

Vlassak, J., & Nix, W., 1992. A new bulge test technique for the determination of Young's modulus and Poisson's ratio of thin films. Journal of Materials Research 7, 3242-3249.

Xiang, Y., Chen, X., Vlassak, J., 2005. Plane-strain Bulge Test for Thin Films. Journal of Materials Research 20, 2360-2370.

Figure captions

Figure 1. (a) Schematic drawing of the internal stress driven on-chip device showing increasing actuator lengths, from left to right. The specimen (shown in light blue) overlaps with the two actuators (shown in dark blue). Boxes are zooms on the corresponding possible crack growth. (b) Fabrication process of an elementary internal-stress-driven mechanical loading structure. (c) 3D illustration of a series of cracking test structures with different actuator lengths. (d) symmetric version of the test configuration.

Figure 2. Description of the generic symmetric and asymmetric test configurations; (a) definition of the geometrical and mechanical parameters; (b) assumption regarding the homogeneity of the applied displacement on the specimen edges; (c) superposition of two problems: actuator contraction and specimen stretching.

Figure 3. Schematics of the four fracture mechanics test specimens that correspond to limit cases of the generic loading configuration of Figure 2; (a) SENT, (b) CCP, (c) DCB1, (d) DCB2.

Figure 4. Variation of $K_I/(1-\nu_a)\sigma_a^{\text{int}}\sqrt{L_a}$ as a function of a/W in the SENT configuration for (a) different E/E_a, L/W=3, W/W_a = 1.5, L_a/L = 5 (full line) or L_a/L = 1 with dotted line, t/t_a = 1, ν_a= 0.3; (b) different W/W_a (but relatively small), E/E_a = 1, L/W = 3, L_a/L = 5, t/t_a = 1, $\nu_a = 0.3$; (c) different L/W, E/E_a = 1, W/W_a = 1.5, L_a/L = 5, t/t_a = 1, $\nu_a = 0.3$.

Figure 5. Variation of $K_I/(1-\nu_a)\sigma_a^{\text{int}}\sqrt{L_a}$ as a function of a/W in the CCP geometry for (a) different E/E_a, L/W=0.1, W/W_a = 10, L_a/L = 5, t/t_a = 1, $\nu_a = 0.3$, (b) different L/W, E/E_a = 1, W/W_a = 10, L_a/L = 5, t/t_a = 1, $\nu_a = 0.3$, (c) different W_a/W, E/E_a = 1, W/W_a = 10, L_a/L = 5, t/t_a = 1, $\nu_a = 0.3$.

Figure 6. Full FE mesh of an asymmetric structure. Inset is a zoomed view of the meshing around the crack tip

Figure 7. Variation of the normalized stress intensity factor $K_I/(1-\nu_a)\sigma_a^{\text{int}}\sqrt{L_a}$ of a SENT configuration as a function of crack length a (normalized by width W) for different levels of internal stress in (a) asymmetric and (b) symmetric configurations. The other parameters have been set equal to L_a/L = 2.5, L/W = 1/6, L_a/W_a = 2.5, t_a/t = 1 and E_a/E = 10 for the symmetric geometry and E_a/E = 1 for the asymmetric geometry.

Figure 8. Variation of the normalized stress intensity factor $K_I/(1-\nu_a)\sigma_a^{\text{int}}\sqrt{L_a}$ with a/W for different L_a/L ratio, for (a) the symmetric and (b) asymmetric configuration. Three types of specimen behaviours are addressed with E_a/E = 1 (continuous line), with E_a/E =10 (dotted lines) and E_a/E = 0.1 (dashed lines). The other parameters have been set equal to L/W = 4/7, t_a/t = 1, W_a/W =4/7 and σ^{int}=0 for (a) and (b).

Figure 9. Variation of the normalized stress intensity factor as a function of a/W for different W_a/W, in the asymmetric configurations for (a) L_a/L=1.25, and (b) L_a/L=20. The other parameters have been set equal to L/W = 4/5, t_a/t = 1, W_a/W=4/5 and σ^{int}=0.

Figure 10. Variation of the normalized stress intensity factor as a function of a/W for no internal stress in the test specimen (dotted line) or a level of internal stress equal to the actuator (continuous line) and different L_a/L, for (a) the symmetric configuration with E_a/E = 1, (b) the asymmetric configuration with E_a/E = 1, (c) the symmetric configuration with E_a/E = 10, (d) the asymmetric configuration with E_a/E = 10, (e) the symmetric configuration with E_a/E = 0.1, (f) the asymmetric configuration with E_a/E = 0.1.

Figure 11. Schematic variation of the value of K_I at cracking initiation, K_{Ic}^{*}, as a function of the initial crack tip opening.

Figure 12. Schematic description of the cracking process starting from notch length for (a) a short actuator length or small internal stress level, (b) cracking process initiated before full release involving unstable cracking and further stable cracking during the end of the release process with subcritical crack growth as time elapses.

Figure 13. Different problems observed when testing the first test structure designs, (a) no propagation, (b) mode III, (c) kinking out of an asymmetric specimen, (d) stiction, (e) kinking out of a symmetric specimen, (f) underetching indicated by white dashed line.

Figure 14. Examples of successful test structures with arrested crack, (a) structure I, inset a zoomed view of the crack tip, (b) structure VI and (c) a 3D view of structure II. The details about these structures are given in the text.

Table

Table 1. Parameters of the SiN structures showing crack arrest, with $\sigma_a^{\text{int}} = 1.11$ GPa and $\nu_a = 0.28$.

Ref. number	L_a^* [μm]	L [μm]	W [μm]	W_a^* [μm]	$t=t_a$ [nm]	a_{c_arrest} [μm]	K_{Ic} [$\text{MPa}\sqrt{\text{m}}$]
I	15 ±1	10 ±1	50 ±2	11 ±0.2	55 ±1	25.5 ±0.2	1.2 ±0.1
II	10 ±1	10 ±1	30 ±2	11 ±0.2	55 ±1	19 ±0.2	1.4 ±0.2
III	10 ±0.3	8 ±0.1	50 ±1	9 ±0.1	55 ±1	14.5 ±0.7	1.8 ±0.1
IV	85 ±4	8.8 ±1	48 ±3	10.25 ±0.3	93 ±1	26.9 ±0.1	1.7 ±0.3
V	62.4 ±4	8.8 ±1	48.3 ±2	10.05 ±0.3	93 ±1	27 ±0.2	1.4 ±0.2
VI	75.5 ±2	9.1 ±1	48.5 ±1	10.25 ±0.1	93 ±1	27.7 ±0.1	1.5 ±0.2
VII	85.9 ±4	9 ±1	48.2 ±4	10.25 ±0.3	93 ±1	28.2 ±0.1	1.6 ±0.3
VIII	53 ±5	8.6 ±1.5	48.5 ±3	10.6 ±0.7	93 ±1	18 ±1	2.9 ±0.1
IX	50 ±6	8.6 ±1.5	48 ±3	10.5 ±0.3	93 ±1	20 ±1.2	2.1 ±0.3
X	53.5 ±5	9.4 ±1	48 ±1	9.8 ±0.3	93 ±1	24.4 ±0.2	1.6 ±0.2
XI	46.1 ±1	9 ±1	44 ±1	9.5 ±0.4	93 ±1	23 ±0.2	1.5 ±0.2
XII	65.2 ±7	9 ±1	35 ±1	9.6 ±0.5	93 ±1	16.5 ±0.3	3.4 ±0.4
XIII	54 ±2	9 ±1	37 ±2	9.55 ±0.3	93 ±1	17.2 ±0.4	2.9 ±0.3
XIV	52.7 ±4	9 ±1	42 ±2	10.3 ±0.3	93 ±1	20.7 ±0.2	2.1 ±0.4
XV	62.5 ±2	9 ±1	39.2 ±1	10.3 ±0.5	93 ±1	21 ±1.5	2.4 ±0.05
$K_{Ic\_mean} = 2 \pm 0.2$ $\text{MPa}\sqrt{\text{m}}$							

Figures

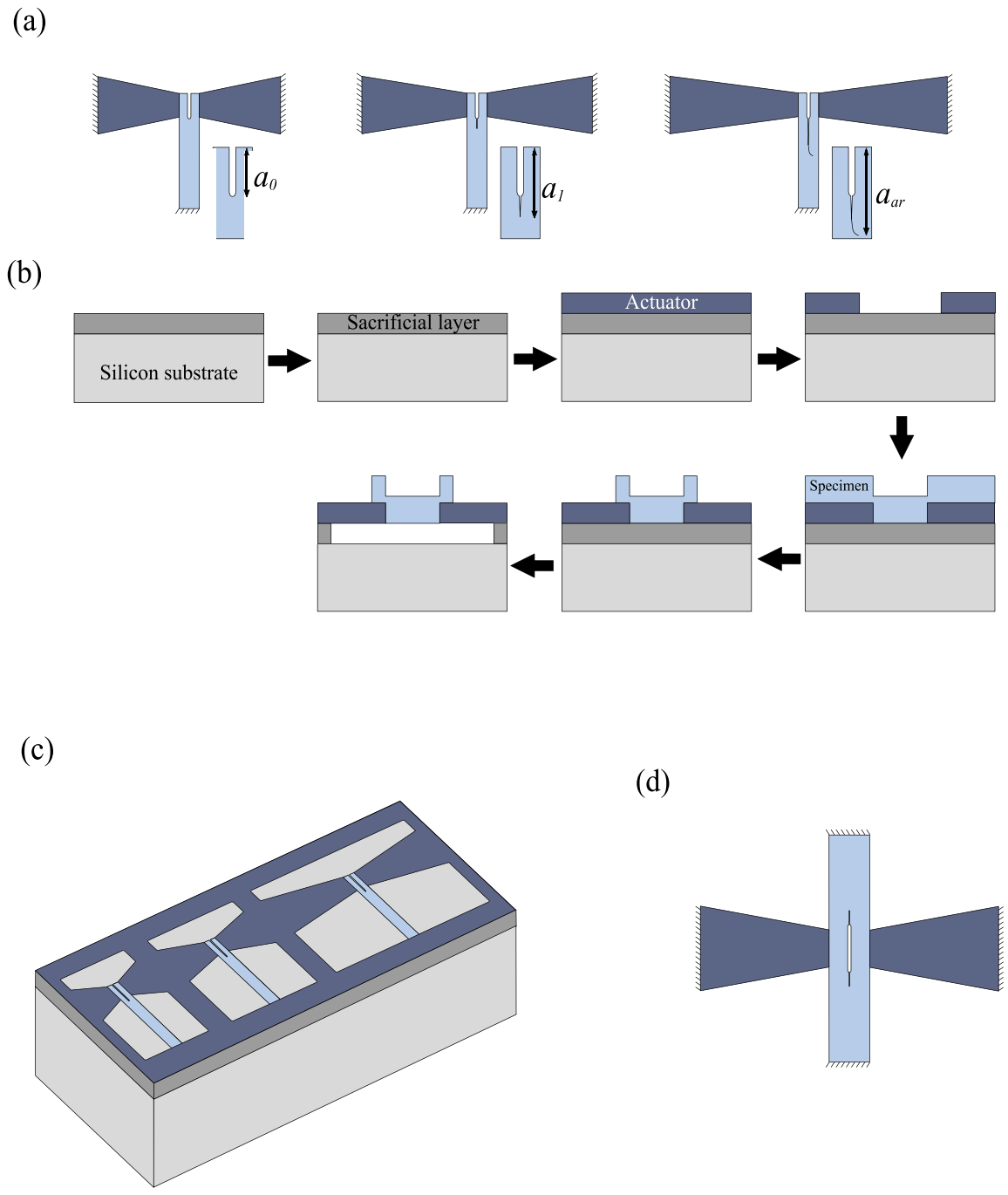

Figure 1. (a) Schematic drawing of the internal stress driven on-chip device showing increasing actuator lengths, from left to right. The specimen (shown in light blue) overlaps with the two actuators (shown in dark blue). Boxes are zooms on the corresponding possible crack growth. (b) Fabrication process of an elementary internal-stress-driven mechanical loading structure. (c) 3D illustration of a series of cracking test structures with different actuator lengths. (d) symmetric version of the test configuration.

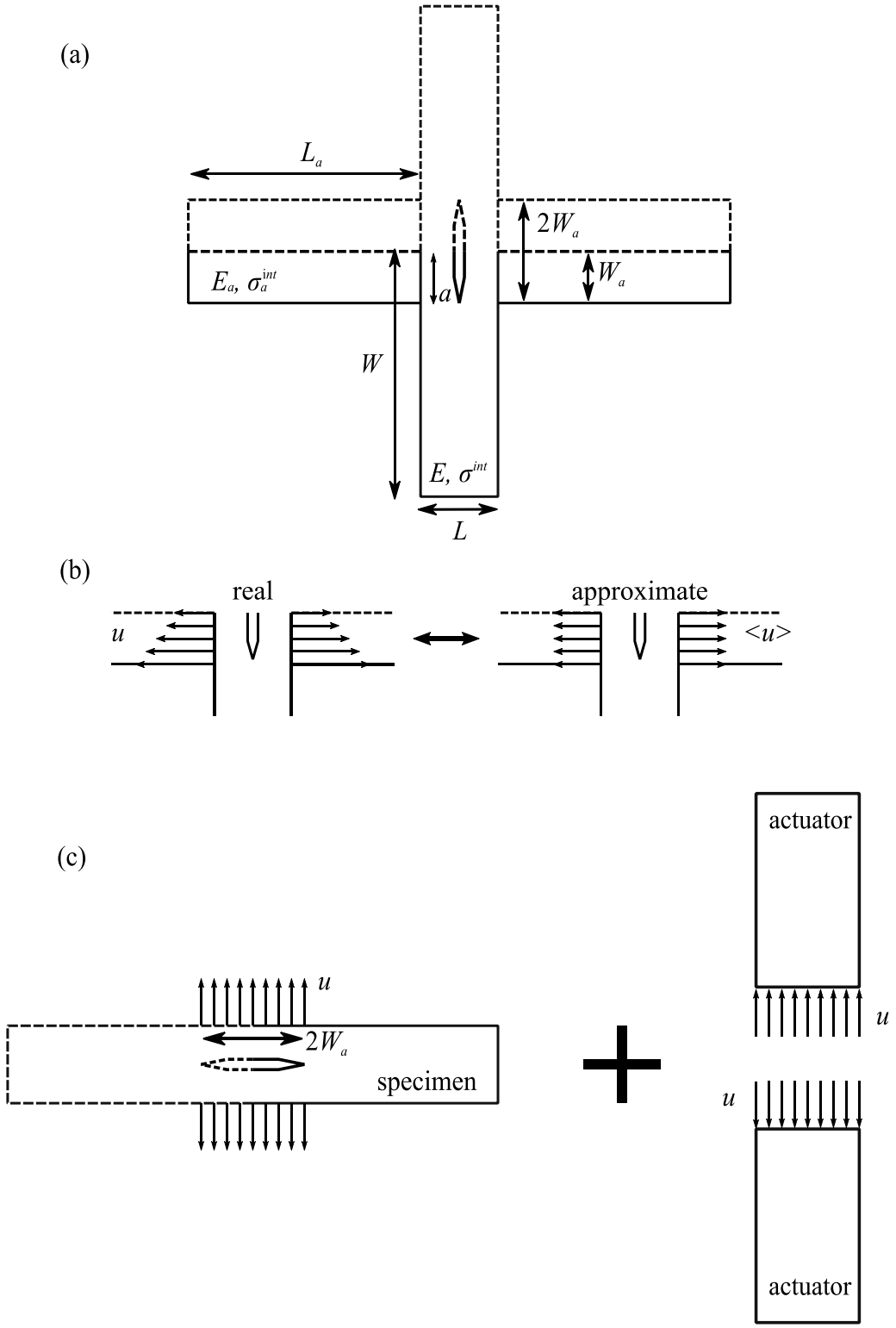

Figure 2. Description of the generic symmetric and asymmetric test configurations; (a) definition of the geometrical and mechanical parameters; (b) assumption regarding the homogeneity of the applied displacement on the specimen edges; (c) superposition of two problems: actuator contraction and specimen stretching.

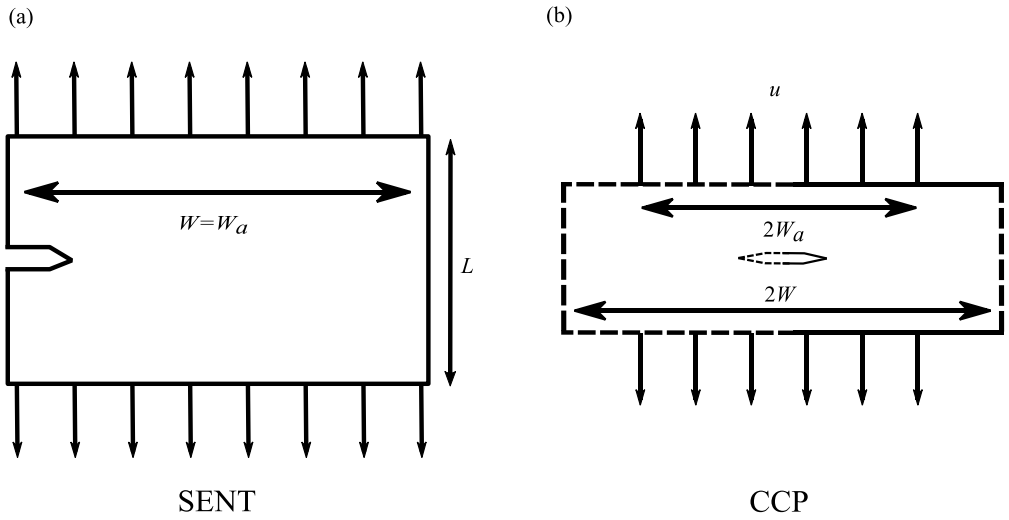

Limit 1: $L \approx W$ & $L < W_a$

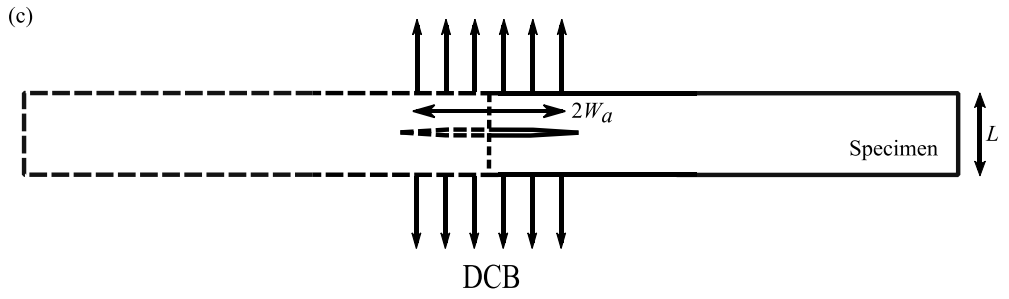

Limit 2: $W_a << W$ & $L << W$

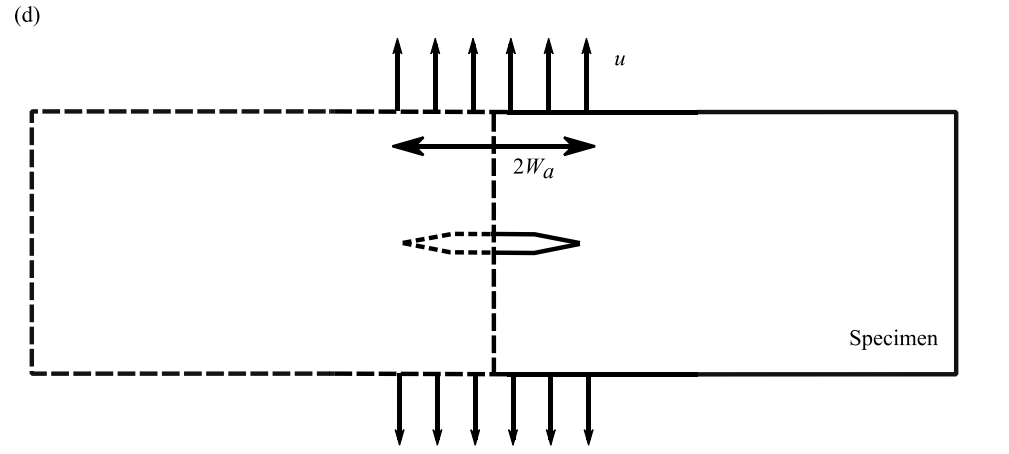

Limit 3: $W_a < W$ & $L \approx W$

Figure 3. Schematics of the four fracture mechanics test specimens that correspond to limit cases of the generic loading configuration of Figure 2; (a) SENT, (b) CCP, (c) DCB1, (d) DCB2.

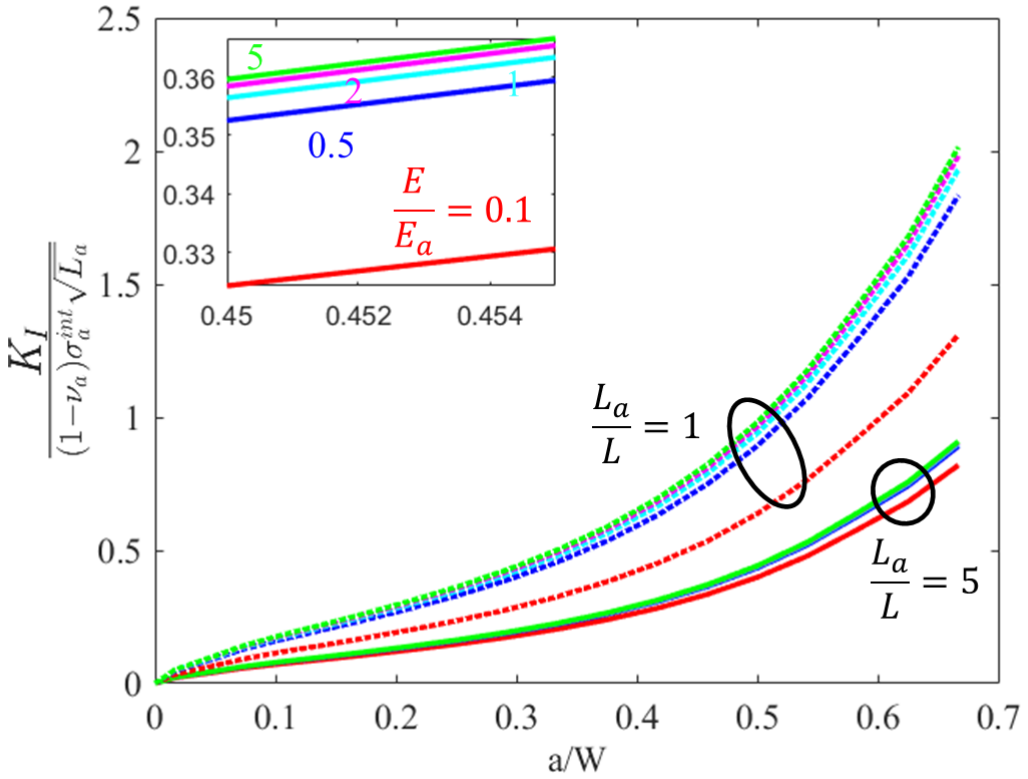
$\frac{K_I}{(1-\nu_a)\sigma_a^{int}\sqrt{L_a}}$
a/W
$\frac{L_a}{L} = 1$
$\frac{L_a}{L} = 5$
$\frac{E}{E_a} = 0.1$
5
2
1
0.5

(a)

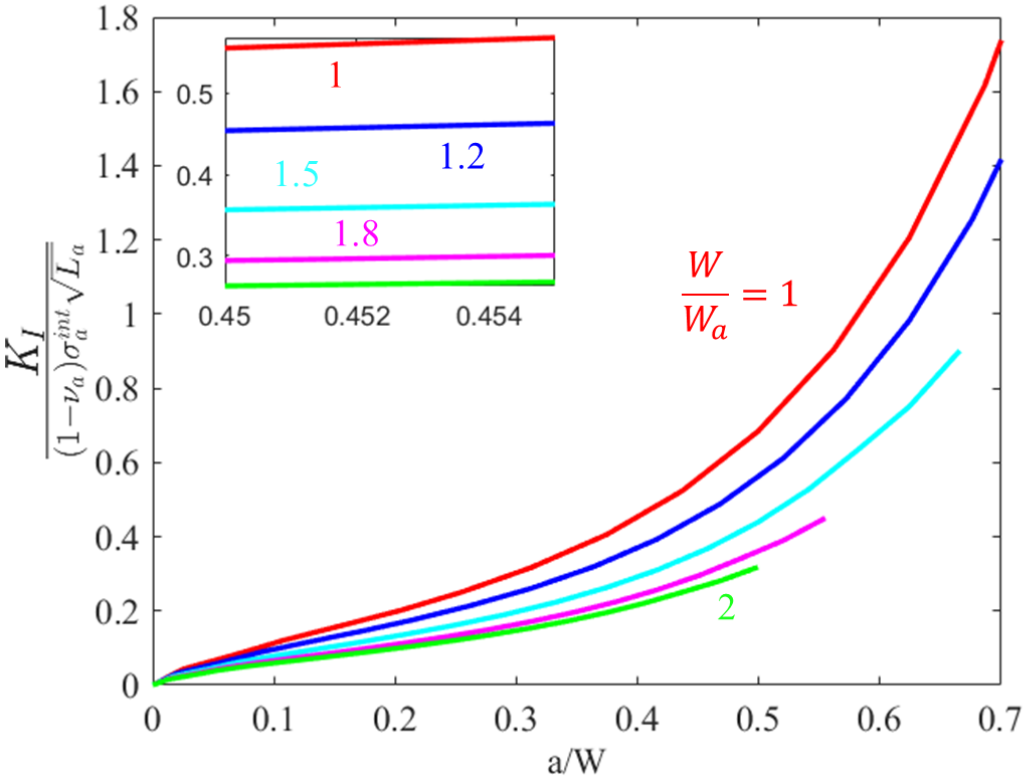
$\frac{K_I}{(1-\nu_a)\sigma_a^{int}\sqrt{L_a}}$
a/W
$\frac{W}{W_a} = 1$
1
1.2
1.5
1.8
2

(b)

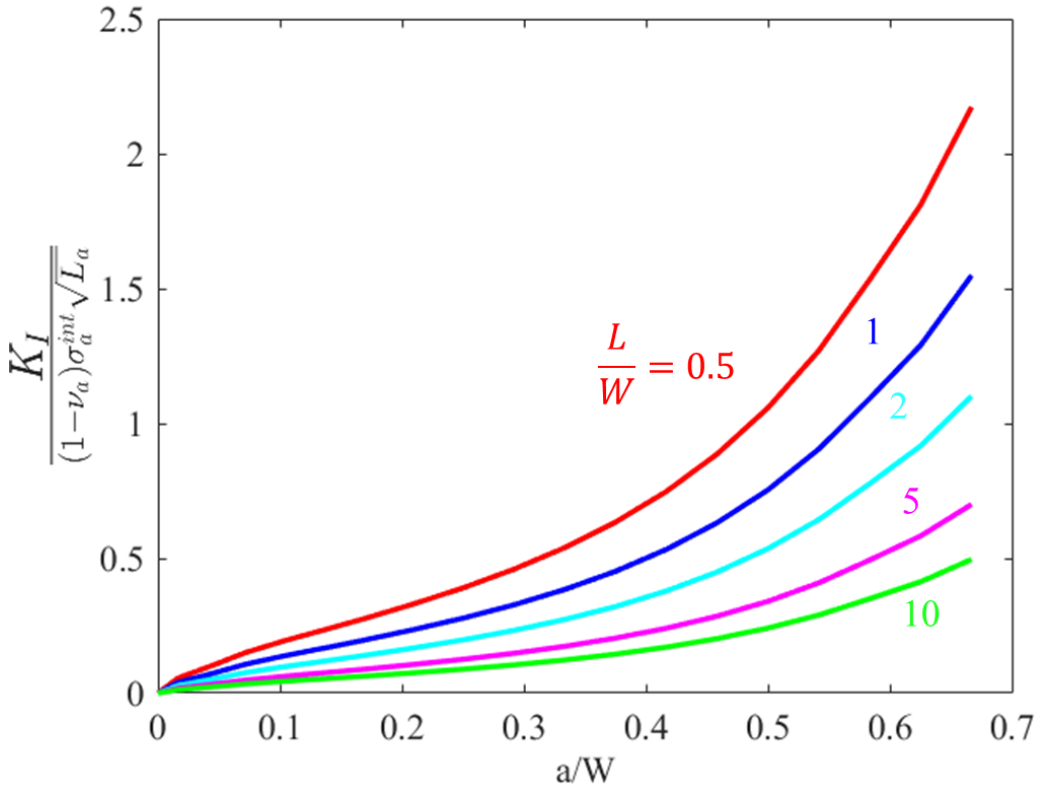

(c)

Figure 4. Variation of $K_I/(1-\nu_a)\sigma_a^{\text{int}}\sqrt{L_a}$ as a function of a/W in the SENT configuration for (a) different E/E_a, L/W=3, W/W_a = 1.5, L_a/L = 5 (full line) or L_a/L = 1 (dotted line), t/t_a = 1, ν_a= 0.3; (b) different W/W_a (but relatively small), E/E_a = 1, L/W = 3, L_a/L = 5, t/t_a = 1, ν_a = 0.3; (c) different L/W, E/E_a = 1, W/W_a = 1.5, L_a/L = 5, t/t_a = 1, ν_a = 0.3.

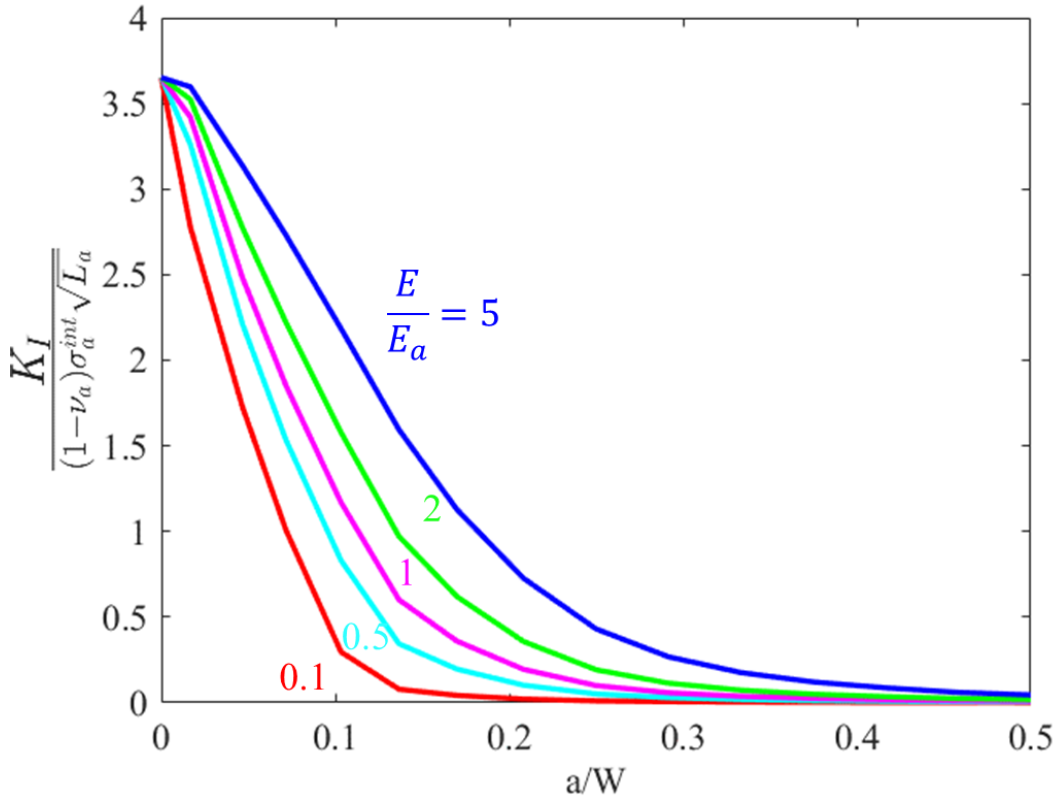
4
3.5
3
2.5
2
1.5
1
0.5
0
0
0.1
0.2
0.3
0.4
0.5
a/W
$\frac{K_I}{(1-\nu_a)\sigma_a^{int}\sqrt{L_a}}$
$\frac{E}{E_a} = 5$
2
1
0.5
0.1

(a)

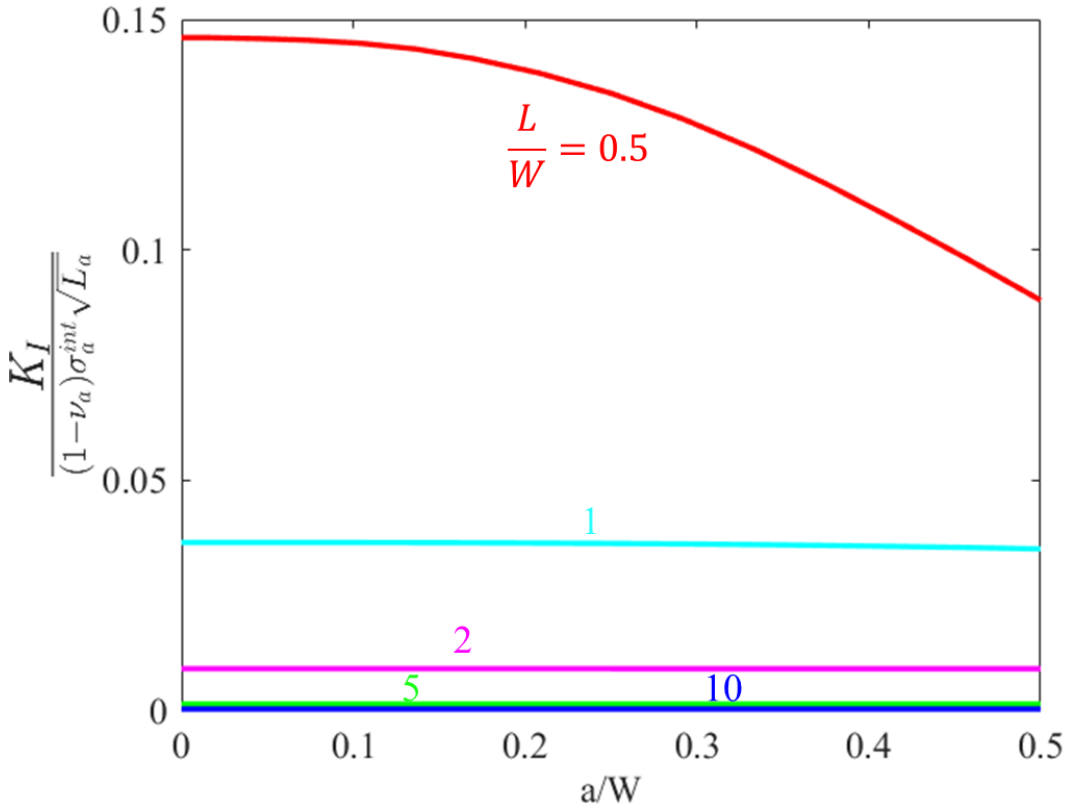
0.15
0.1
0.05
0
0
0.1
0.2
0.3
0.4
0.5
a/W
$\frac{K_I}{(1-\nu_a)\sigma_a^{int}\sqrt{L_a}}$
$\frac{L}{W} = 0.5$
1
2
5
10

(b)

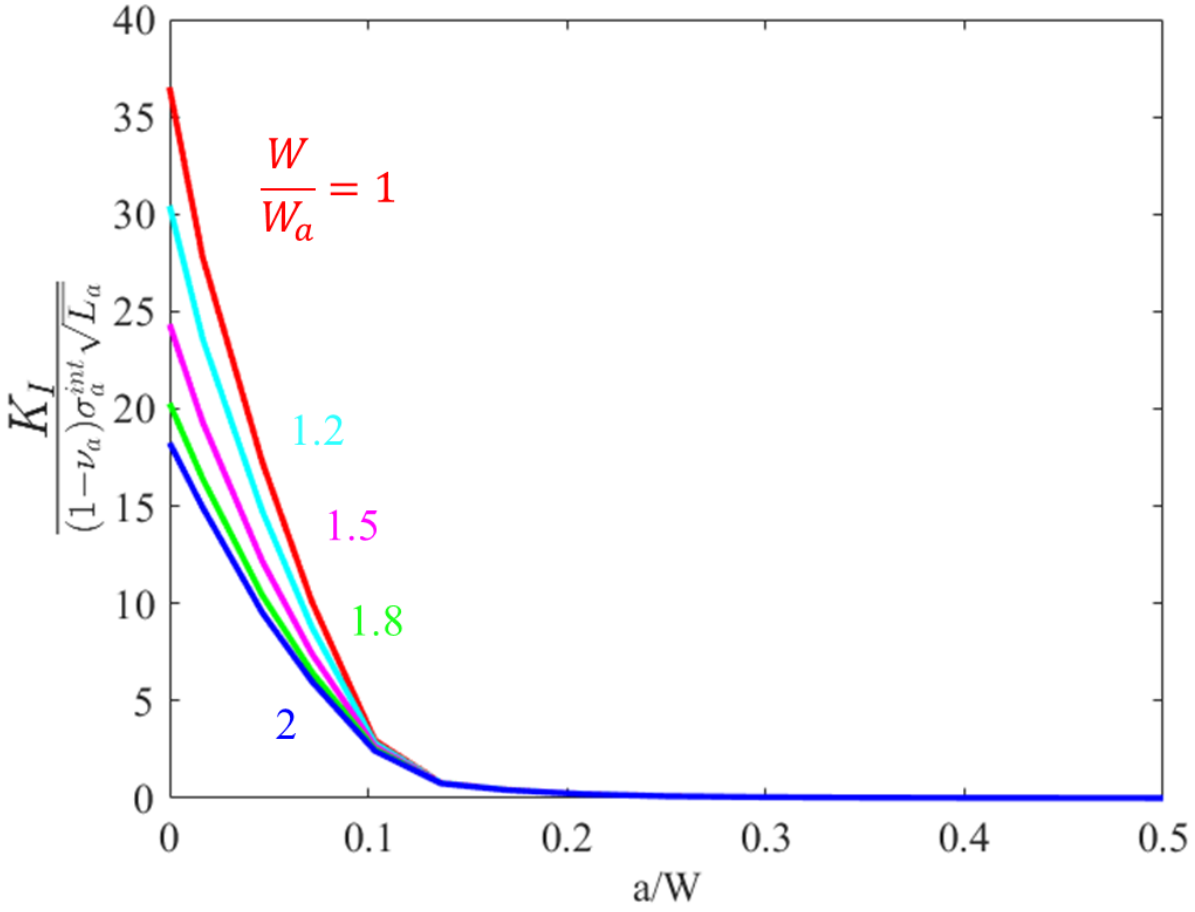

(c)

Figure 5. Variation of $K_I/(1-\nu_a)\sigma_a^{\text{int}}\sqrt{L_a}$ as a function of *a/W* in the CCP geometry for (a) different E/E_a, L/W=0.1, W/W_a = 10, L_a/L = 5, t/t_a = 1, ν_a = 0.3, (b) different L/W, E/E_a = 1, W/W_a = 10, L_a/L = 5, t/t_a = 1, ν_a = 0.3, (c) different W_a/W, E/E_a = 1, W/W_a = 10, L_a/L = 5, t/t_a = 1, ν_a = 0.3.

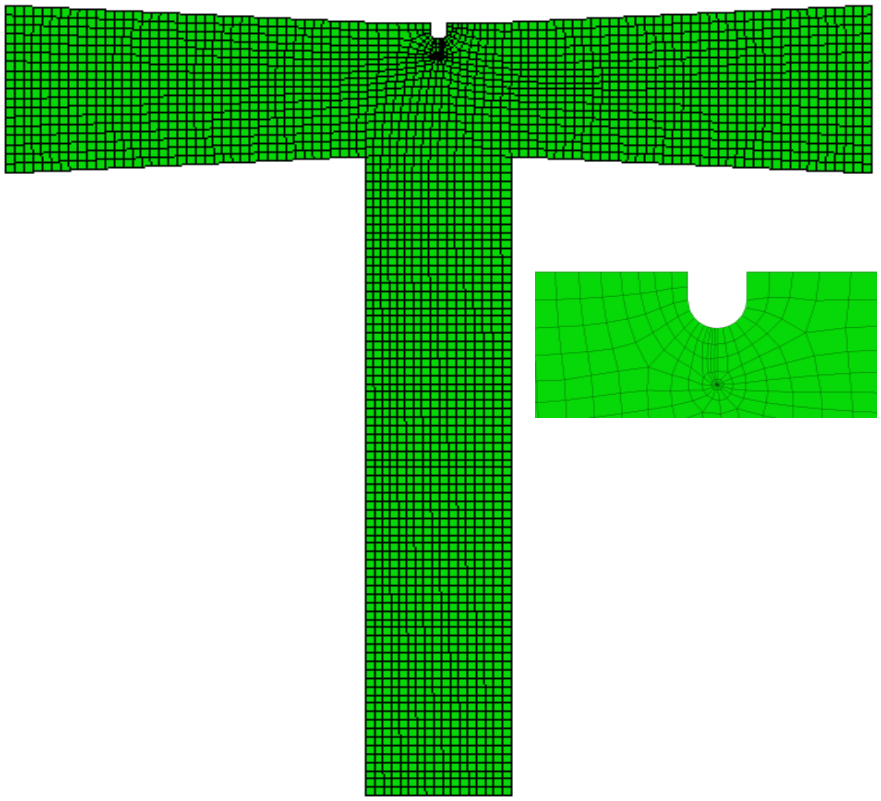

Figure 6. Full FE mesh of an asymmetric structure. Inset is a zoomed view of the meshing around the crack tip

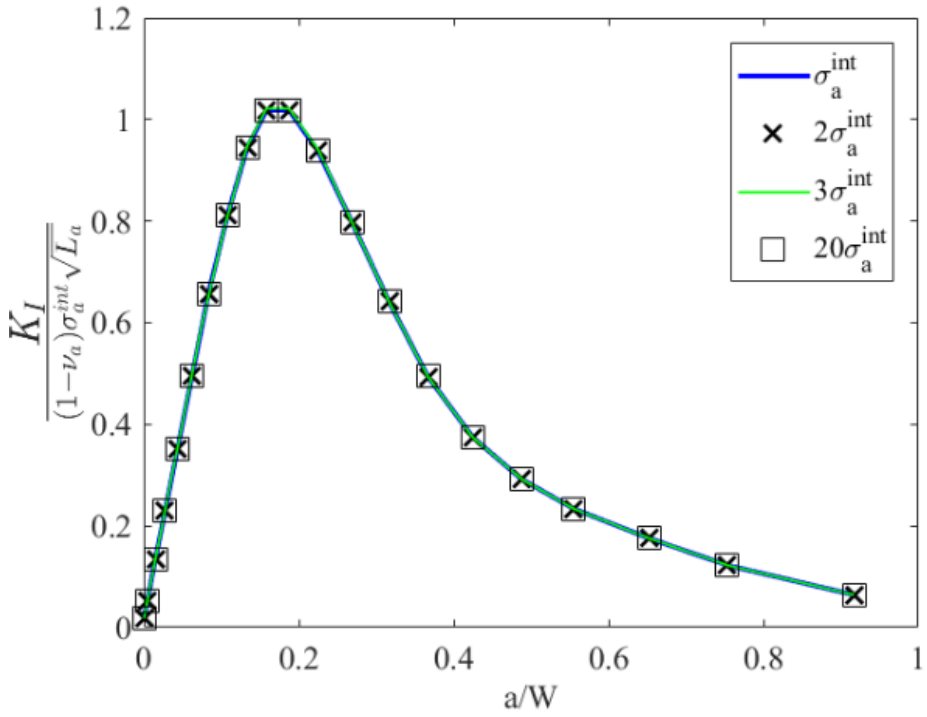

(a)

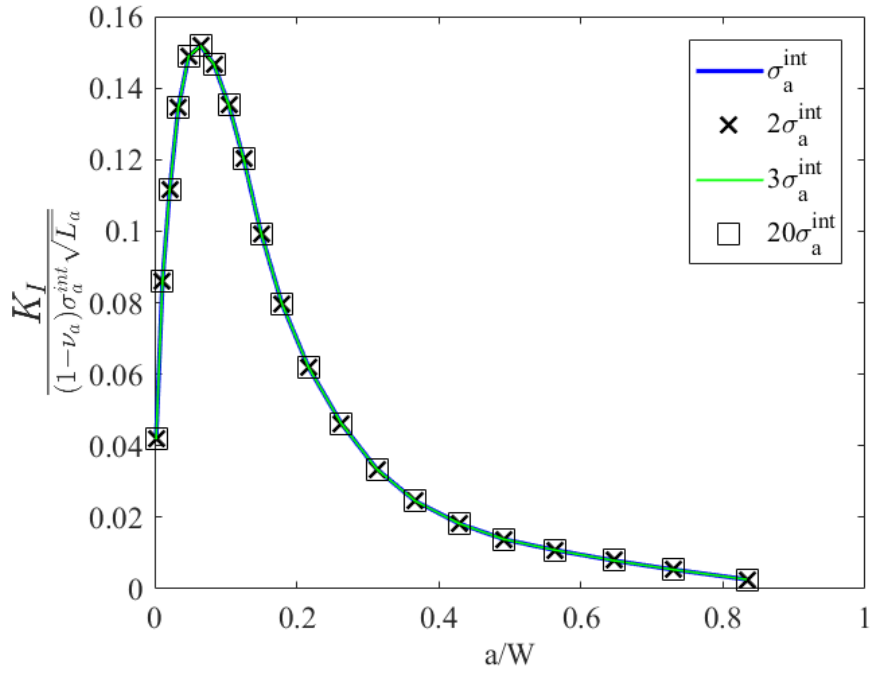

(b)

Figure 7. Variation of the normalized stress intensity factor $K_I/(1-\nu_a)\sigma_a^{int}\sqrt{L_a}$ of a SENT configuration as a function of crack length a (normalized by width W) for different levels of internal stress in (a) asymmetric and (b) symmetric configurations. The other parameters have been set equal to L_a/L = 2.5, L/W = 1/6, L_a/W_a = 2.5, t_a/t = 1 and E_a/E = 10 for the symmetric geometry and E_a/E = 1 for the asymmetric geometry.

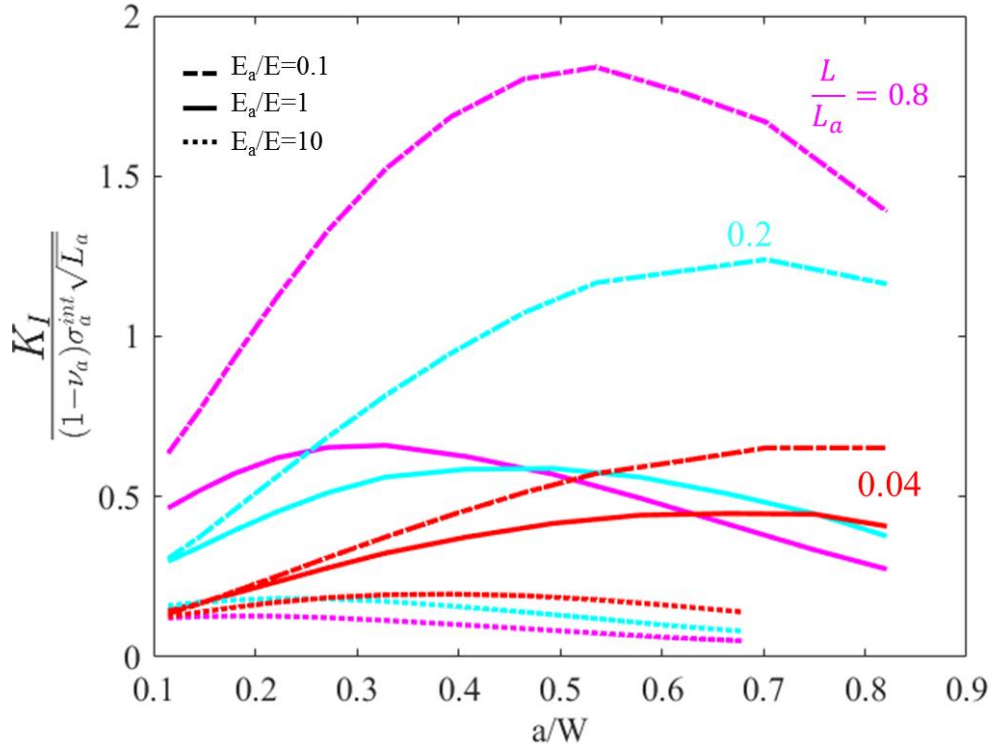

(a)

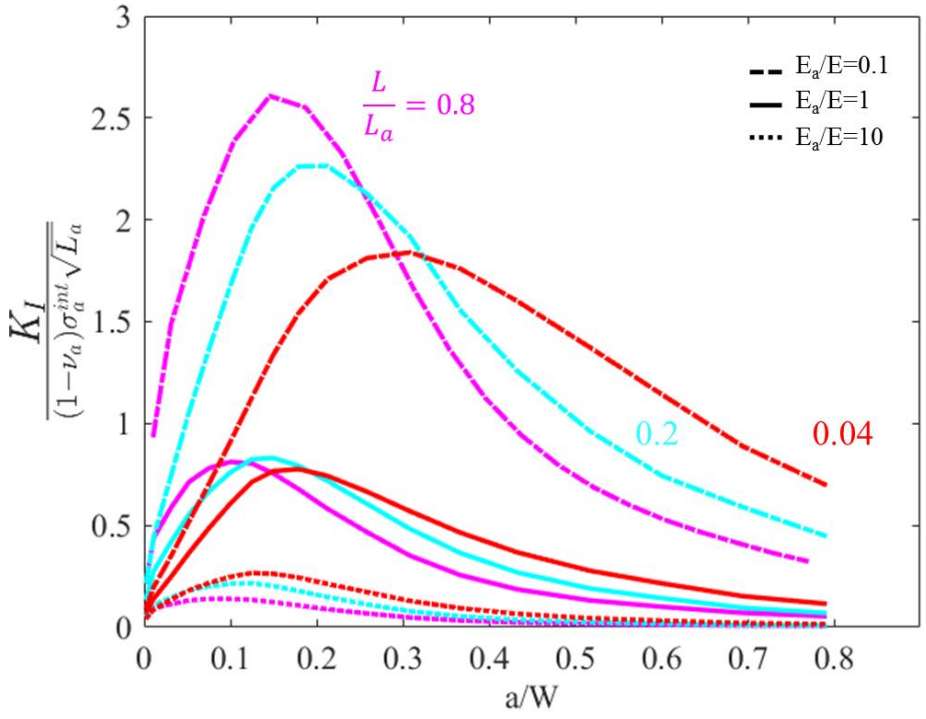

(b)

Figure 8. Variation of the normalized stress intensity factor $K/(1-\nu_a)\sigma_a^{int}\sqrt{L_a}$ with a/W for different L_a/L ratio, for (a) the symmetric and (b) asymmetric configuration. Three types of specimen behaviours are addressed with E_a/E = 1 (continuous line), with E_a/E =10 (dotted lines) and E_a/E = 0.1 (dashed lines). The other parameters have been set equal to L/W = 4/7, t_a/t = 1, W_a/W =4/7 and σ^{int}=0 for (a) and (b).

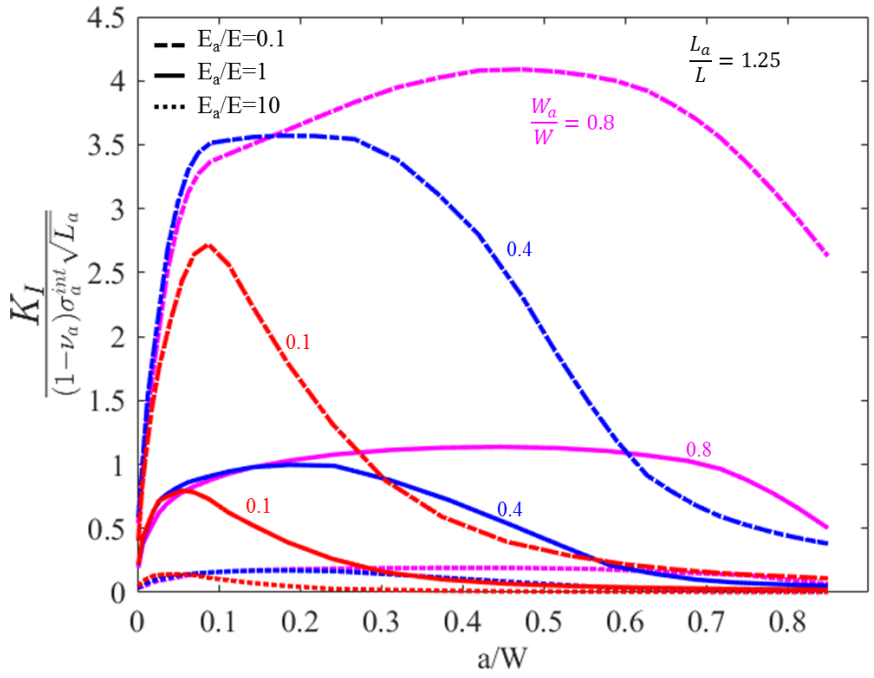

(a)

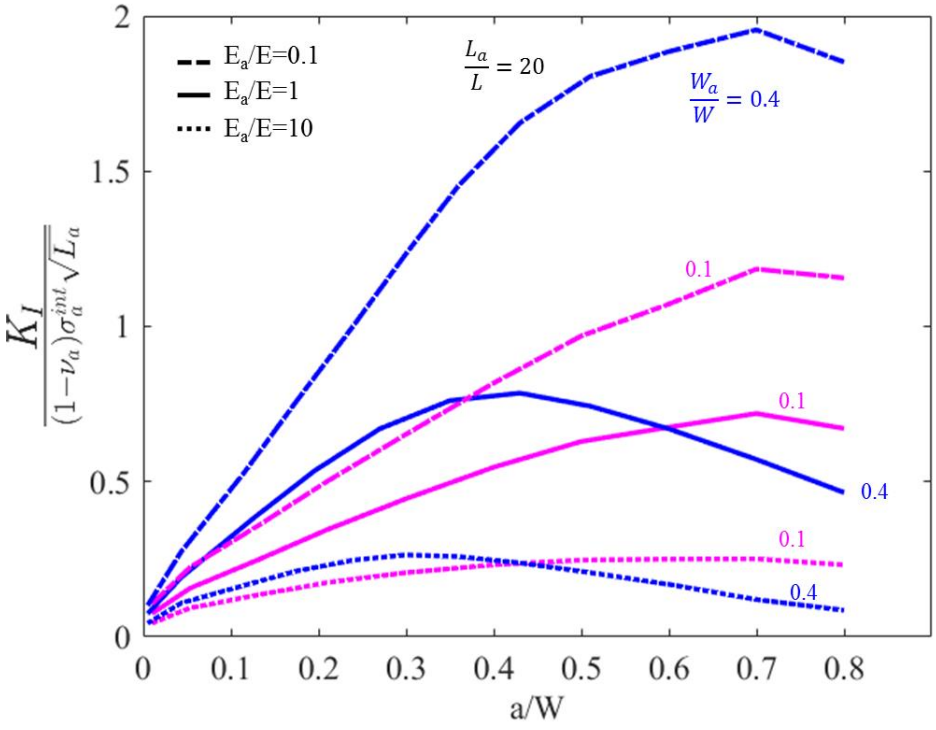

(b)

Figure 9. Variation of the normalized stress intensity factor as a function of a/W for different W_a/W, in the asymmetric configurations for (a) L_a/L=1.25, and (b) L_a/L=20. The other parameters have been set equal to L/W = 4/5, t_a/t = 1, W_a/W=4/5 and σ^{int}=0.

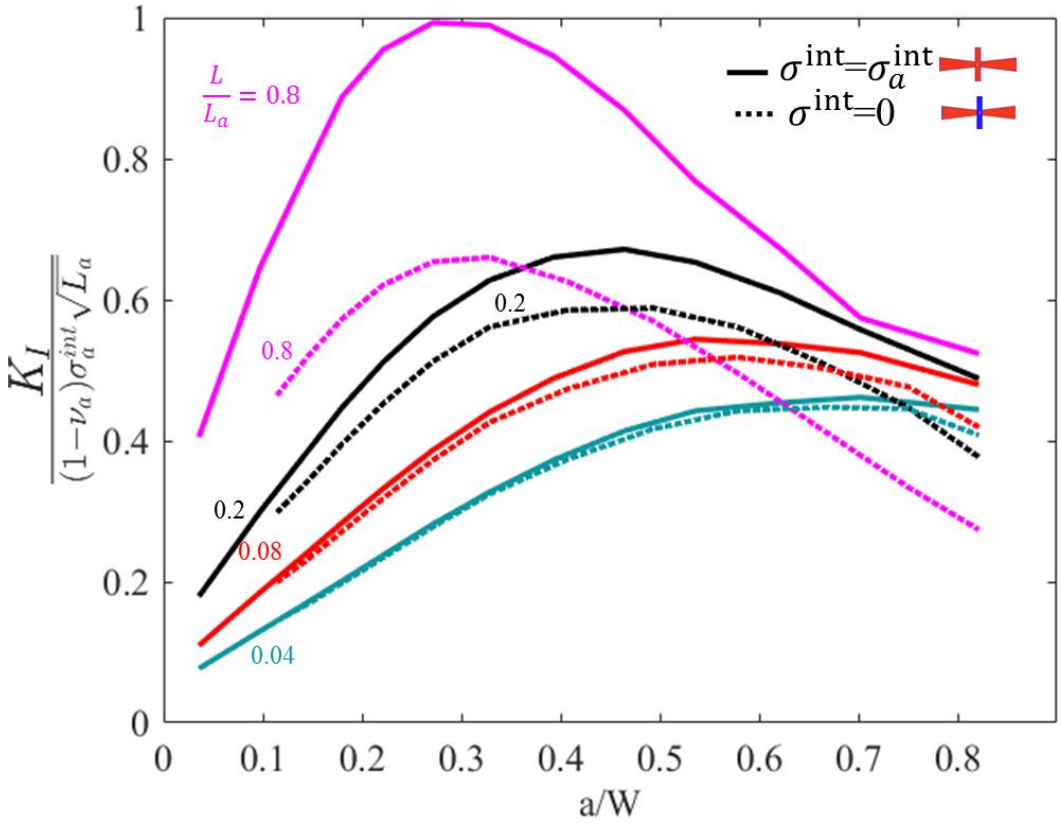
$\frac{L}{L_a} = 0.8$
$\sigma^{int}=\sigma_a^{int}$
$\sigma^{int}=0$
0.8
0.2
0.2
0.08
0.04
$\frac{K_I}{(1-\nu_a)\sigma_a^{int}\sqrt{L_a}}$
a/W

(a)

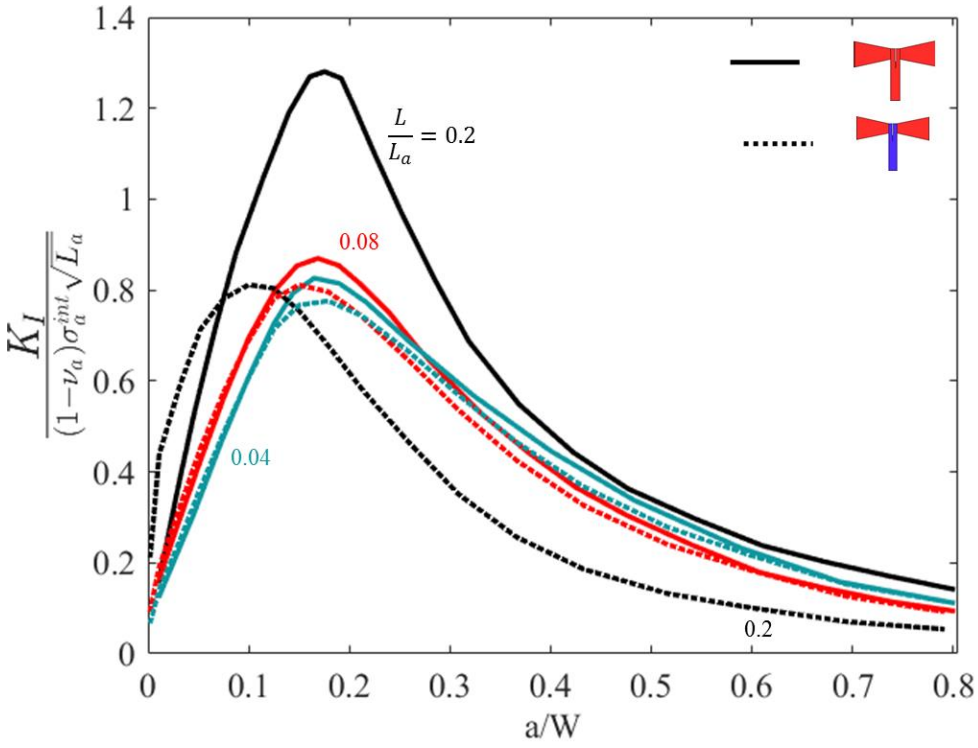
$\frac{L}{L_a} = 0.2$
0.08
0.04
0.2
$\frac{K_I}{(1-\nu_a)\sigma_a^{int}\sqrt{L_a}}$
a/W

(b)

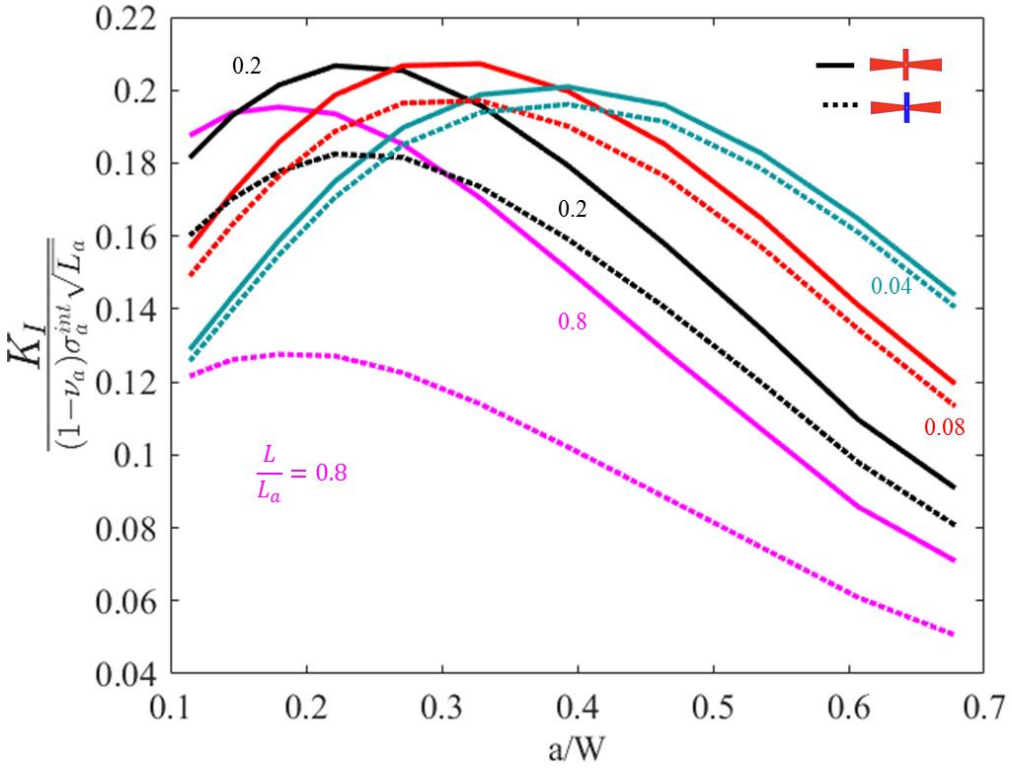
0.22
0.2
0.18
0.16
0.14
0.12
0.1
0.08
0.06
0.04
0.1
0.2
0.3
0.4
0.5
0.6
0.7
a/W
$\frac{K_I}{(1-\nu_a)\sigma_a^{int}\sqrt{L_a}}$
0.2
0.2
0.04
0.8
0.08
$\frac{L}{L_a} = 0.8$

(c)

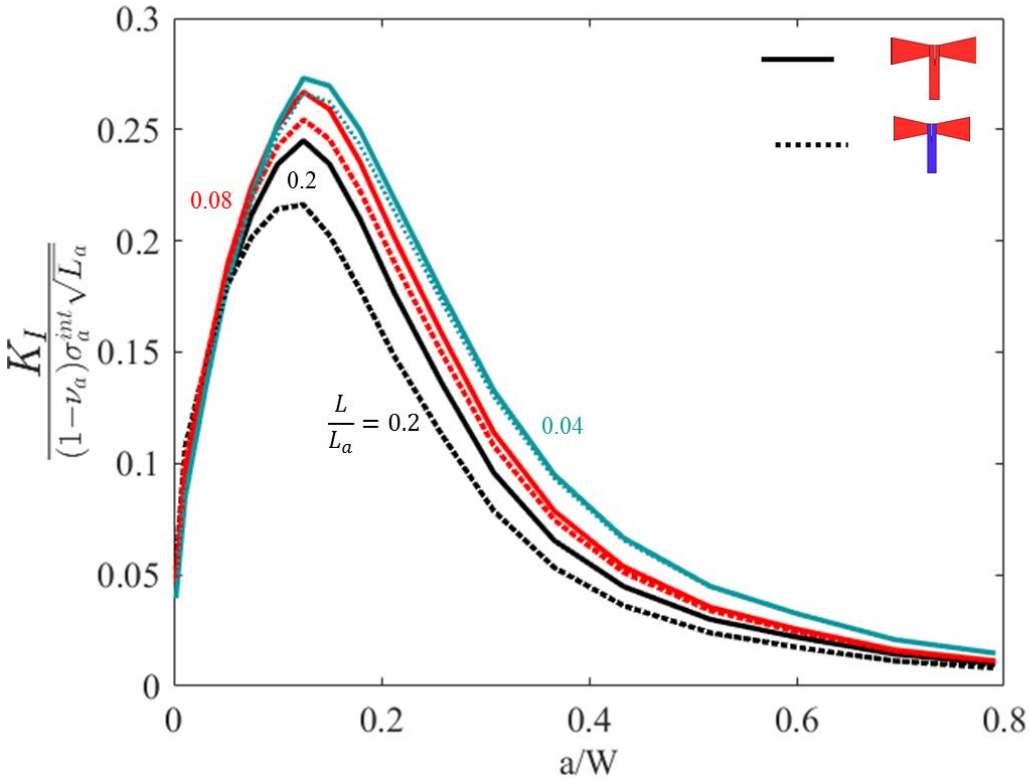
0.3
0.25
0.2
0.15
0.1
0.05
0
0
0.2
0.4
0.6
0.8
a/W
$\frac{K_I}{(1-\nu_a)\sigma_a^{int}\sqrt{L_a}}$
0.08
0.2
$\frac{L}{L_a} = 0.2$
0.04

(d)

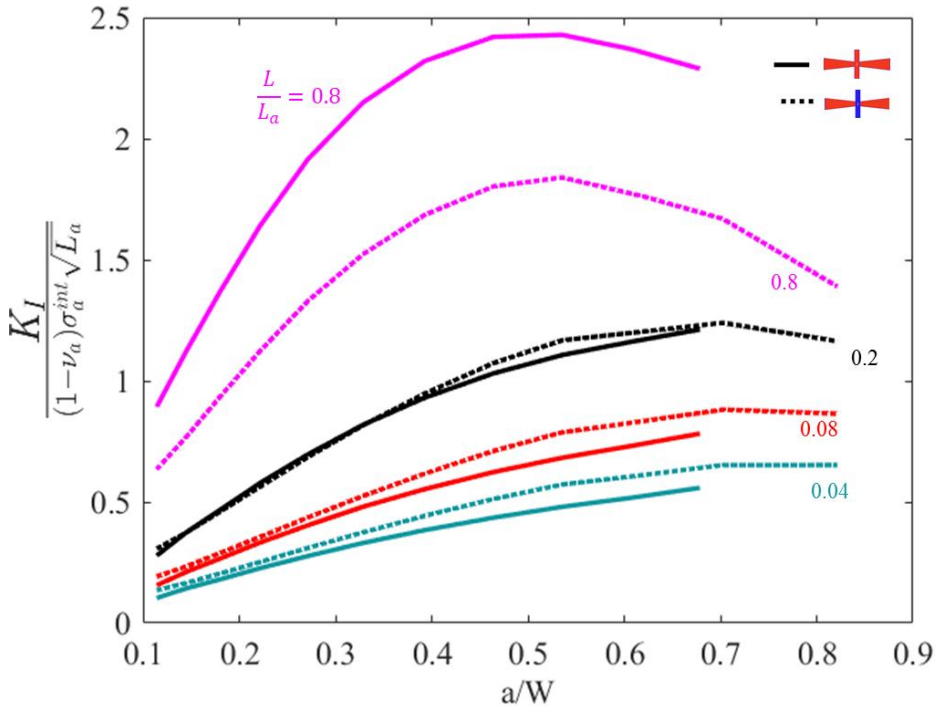

(e)

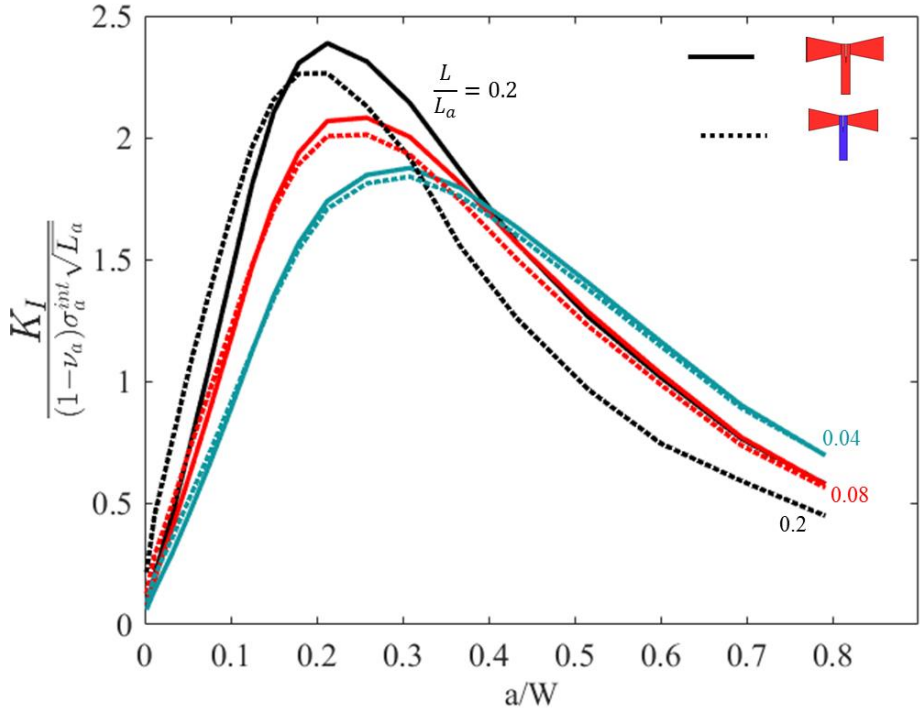

(f)

Figure 10. Variation of the normalized stress intensity factor as a function of *a/W* for no internal stress in the test specimen (dotted line) or a level of internal stress equal to the actuator (continuous line) and different L_a/L, for (a) the symmetric configuration with $E_a/E = 1$, (b) the asymmetric configuration with $E_a/E = 1$, (c) the symmetric configuration with $E_a/E = 10$, (d) the asymmetric configuration with $E_a/E = 10$, (e) the symmetric configuration with $E_a/E = 0.1$, (f) the asymmetric configuration with $E_a/E = 0.1$.

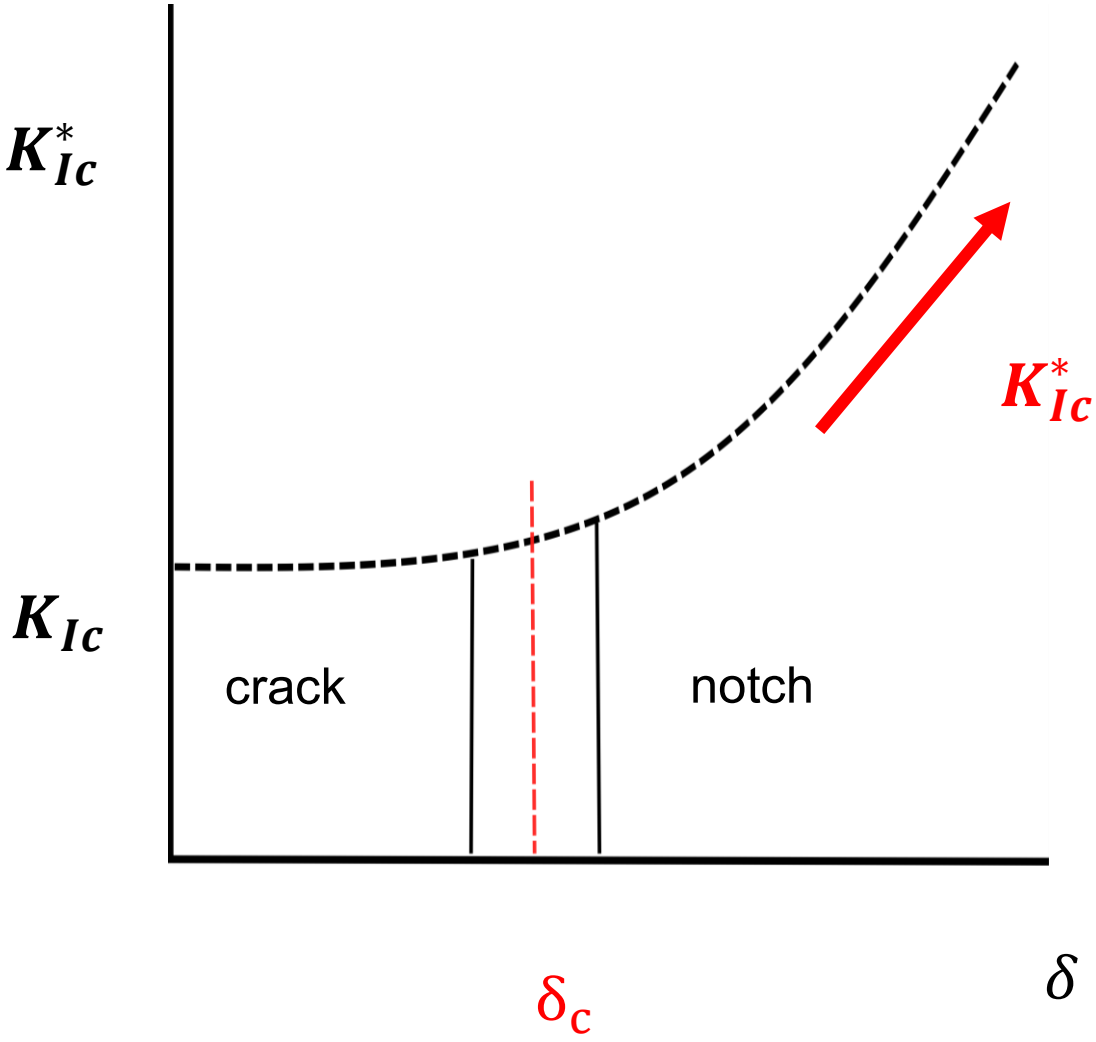

Figure 11. Schematic variation of the value of K_I at cracking initiation, K_{Ic}^{*}, as a function of the initial crack tip opening.

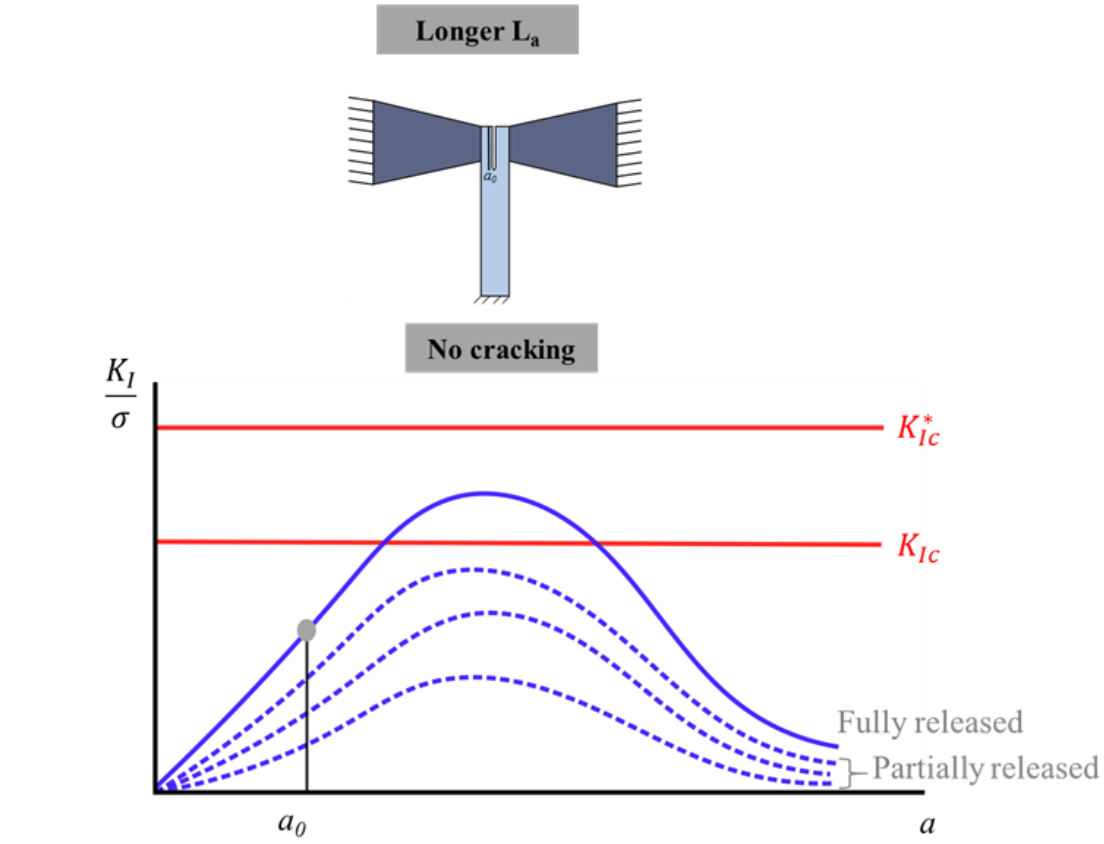

(a)

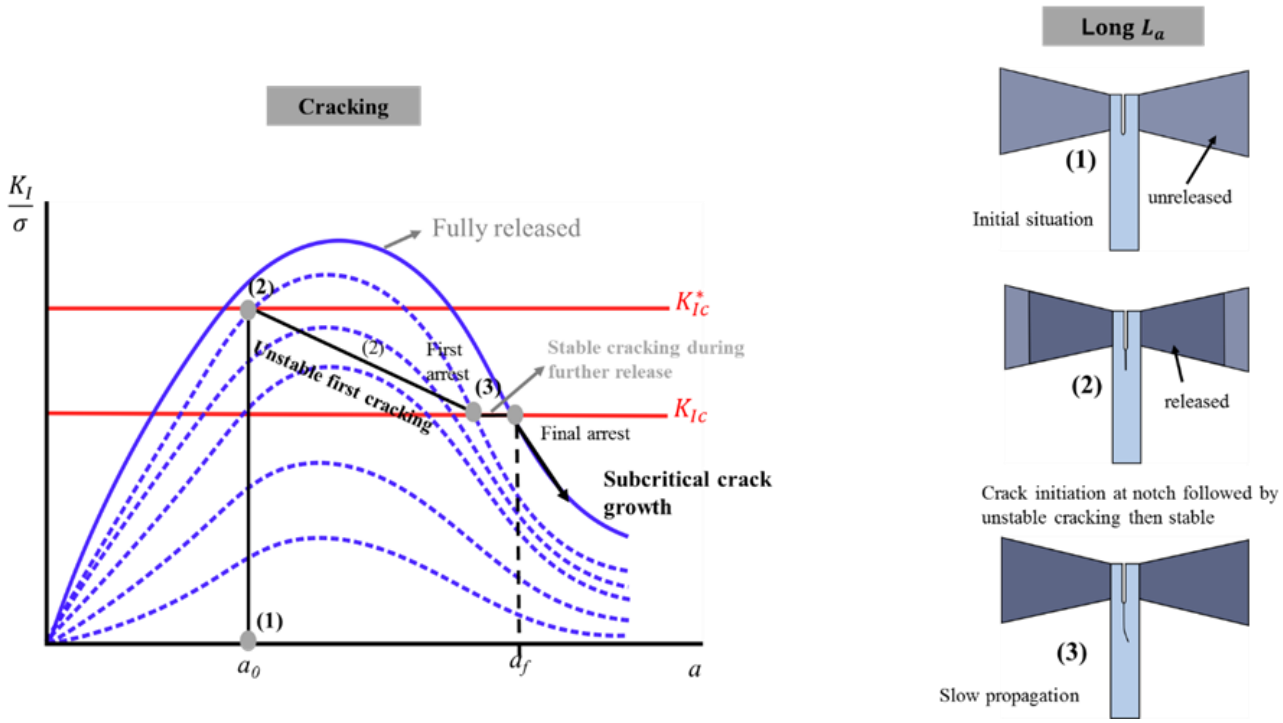

(b)

Figure 12. Schematic description of the cracking process starting from notch length for (a) a short actuator length or small internal stress level, (b) cracking process initiated before full release involving unstable cracking and further stable cracking during the end of the release process with subcritical crack growth as time elapses.

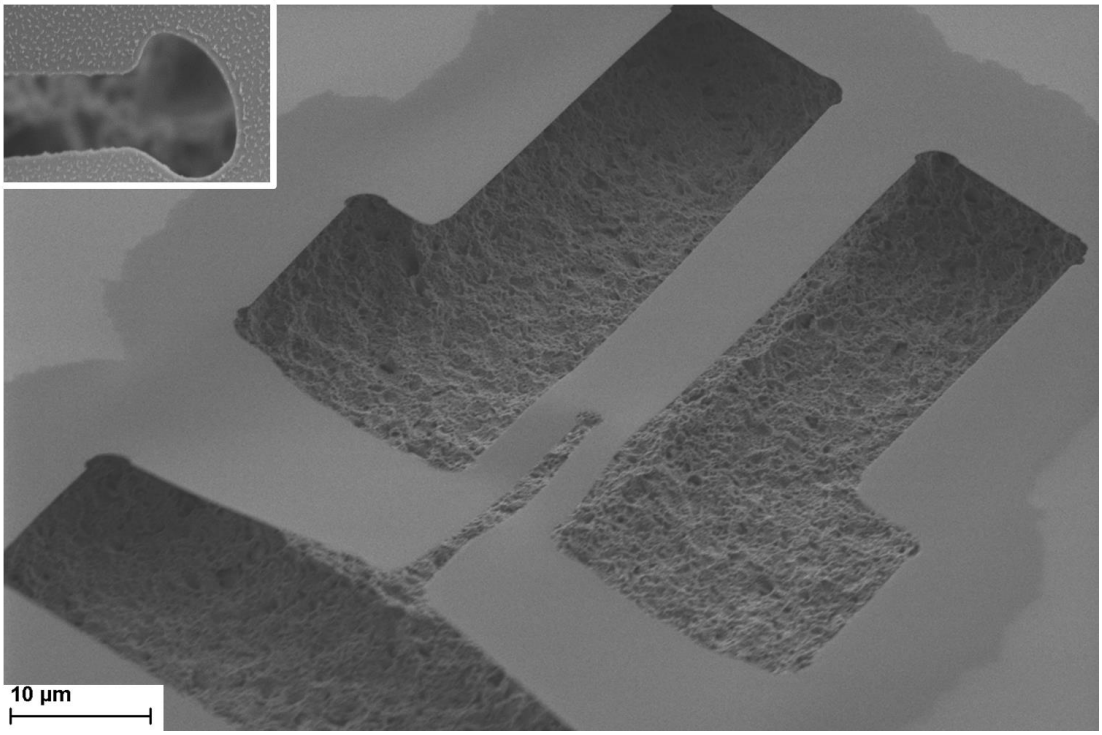

(a)

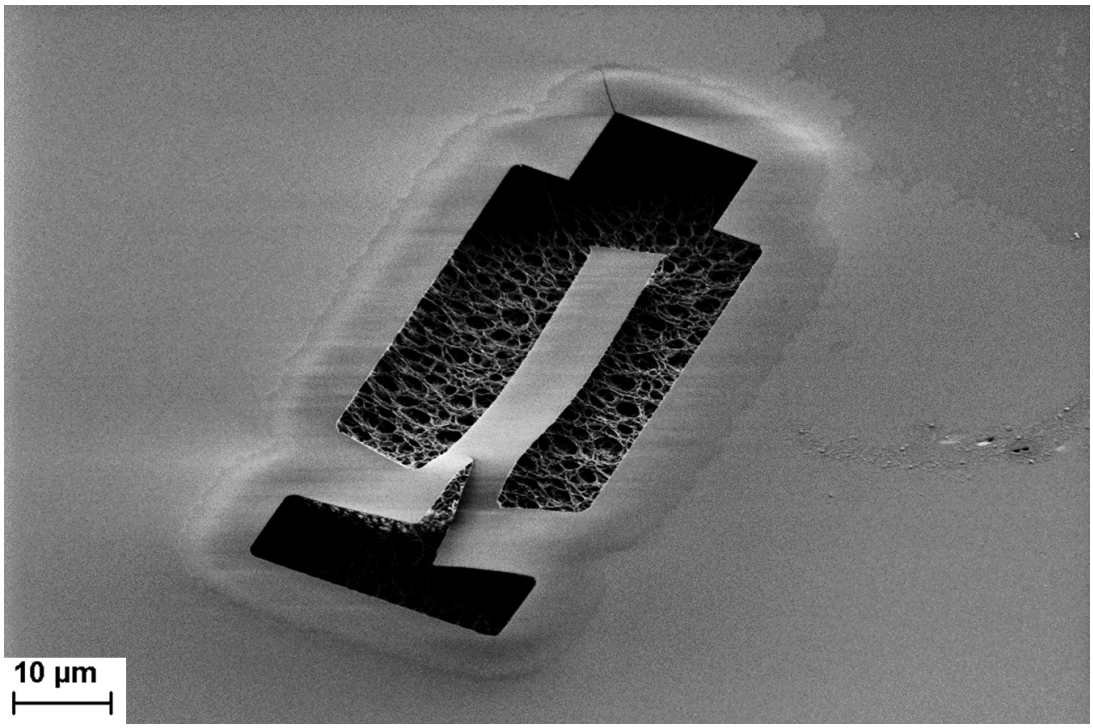

(b)

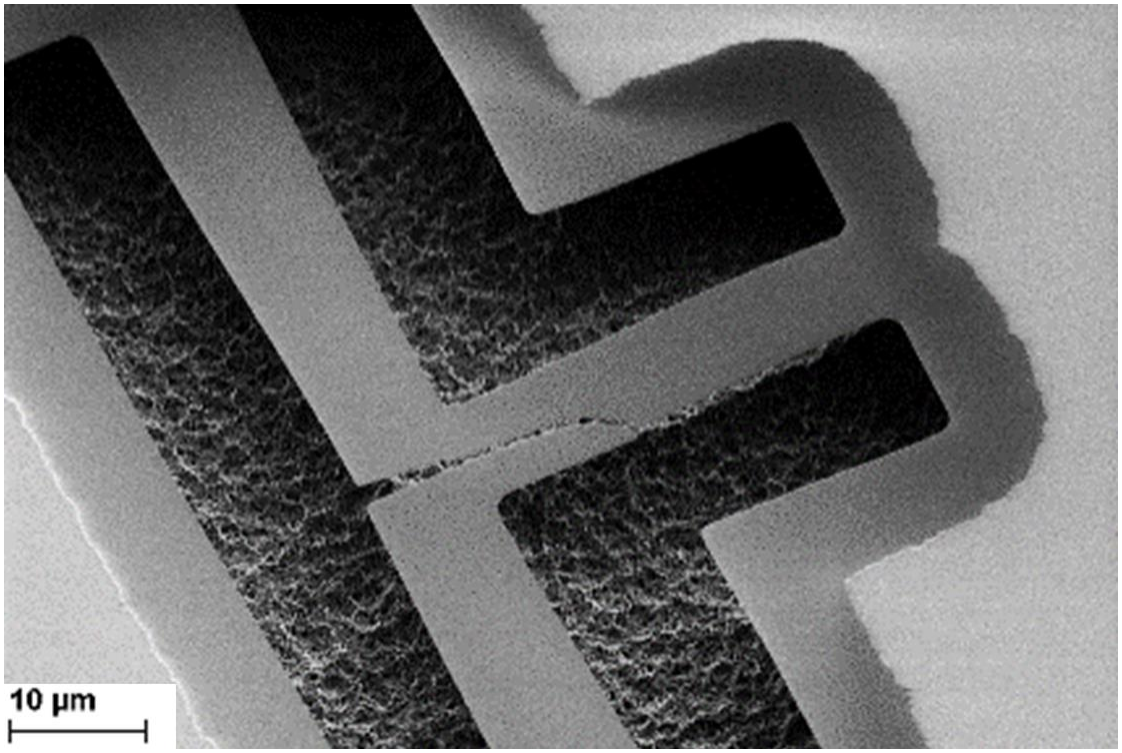

(c)

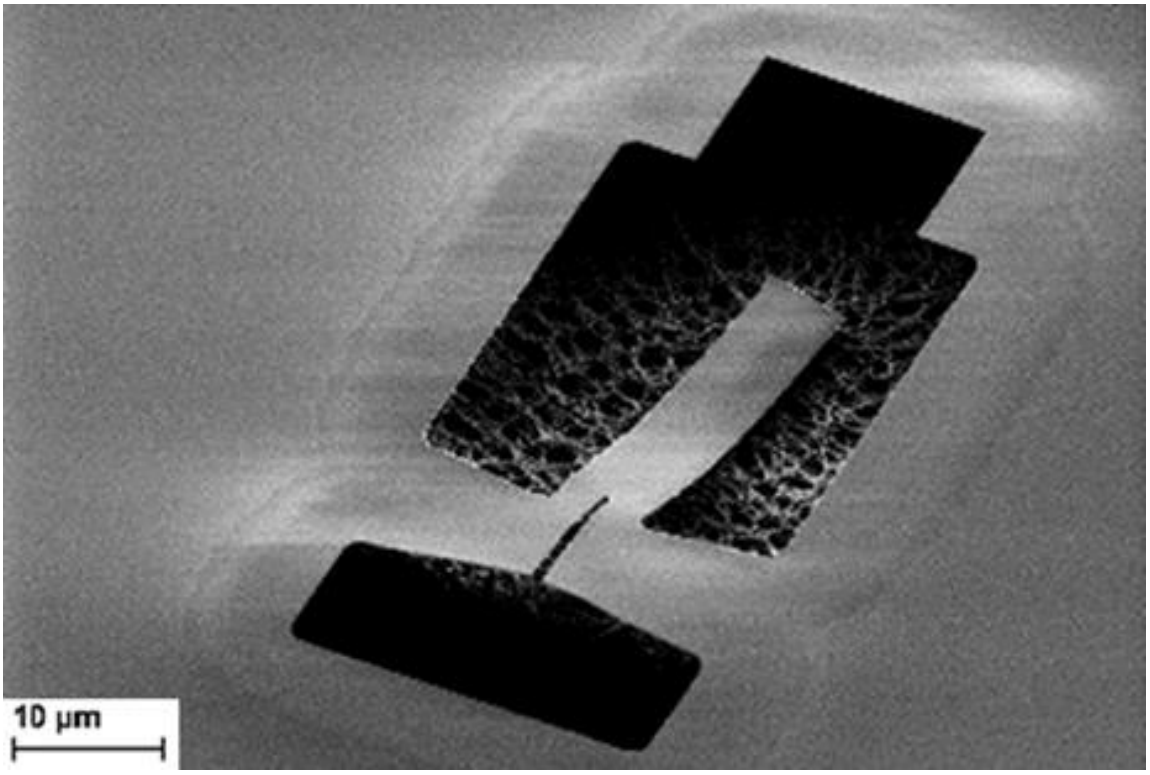

(d)

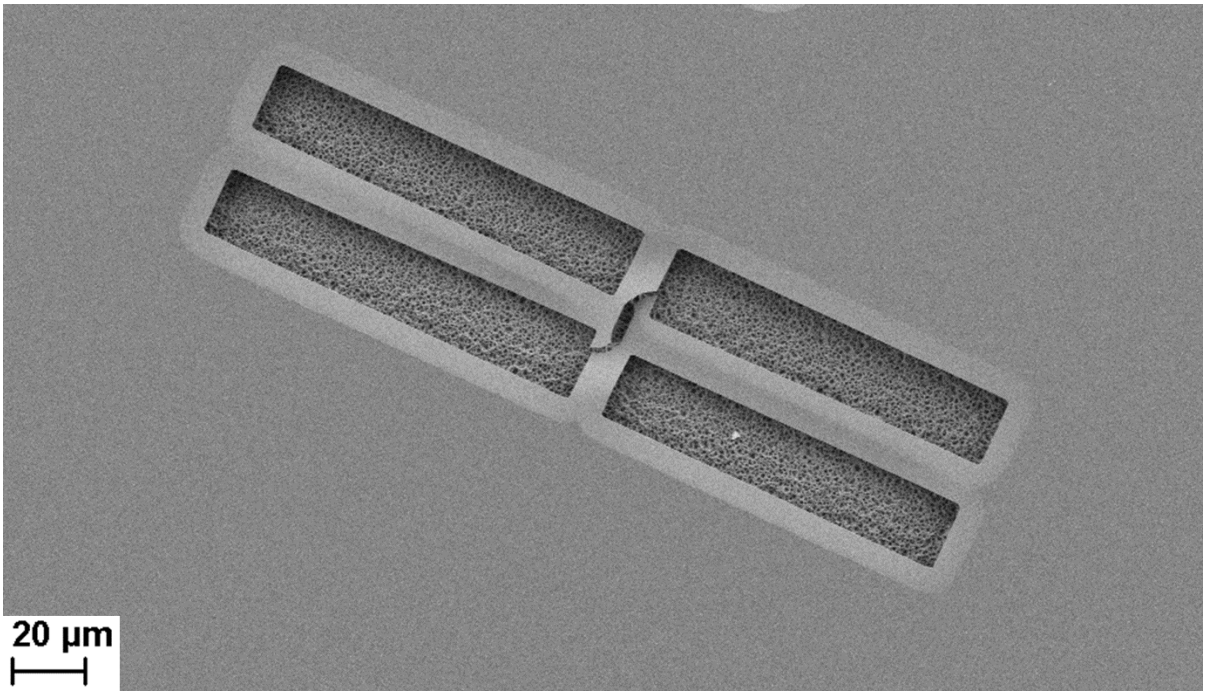

(e)

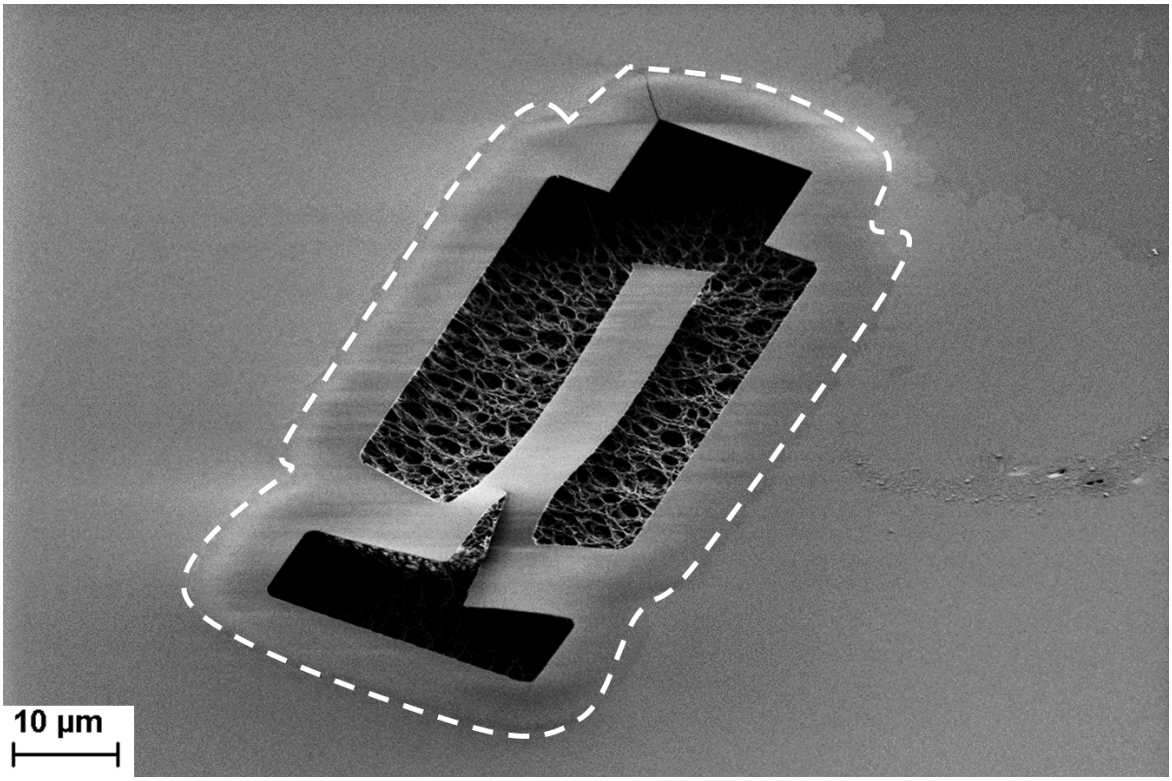

(f)

Figure 13. Different problems observed when testing the first test structure designs, (a) no propagation, (b) mode III, (c) kinking out of an asymmetric specimen, (d) stiction, (e) kinking out of a symmetric specimen, (f) underetching indicated by white dashed line.

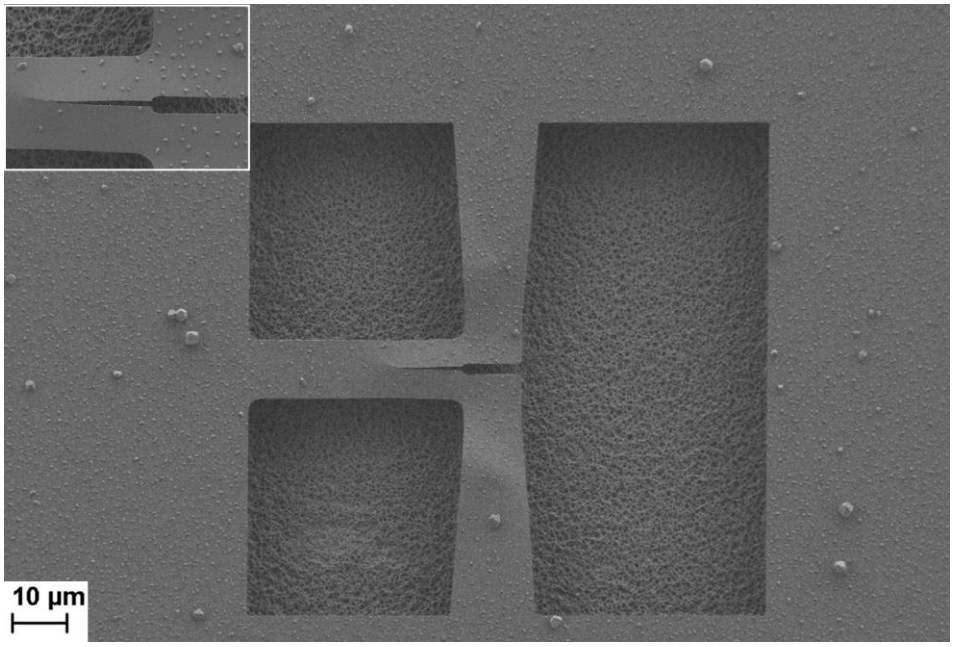

(a)

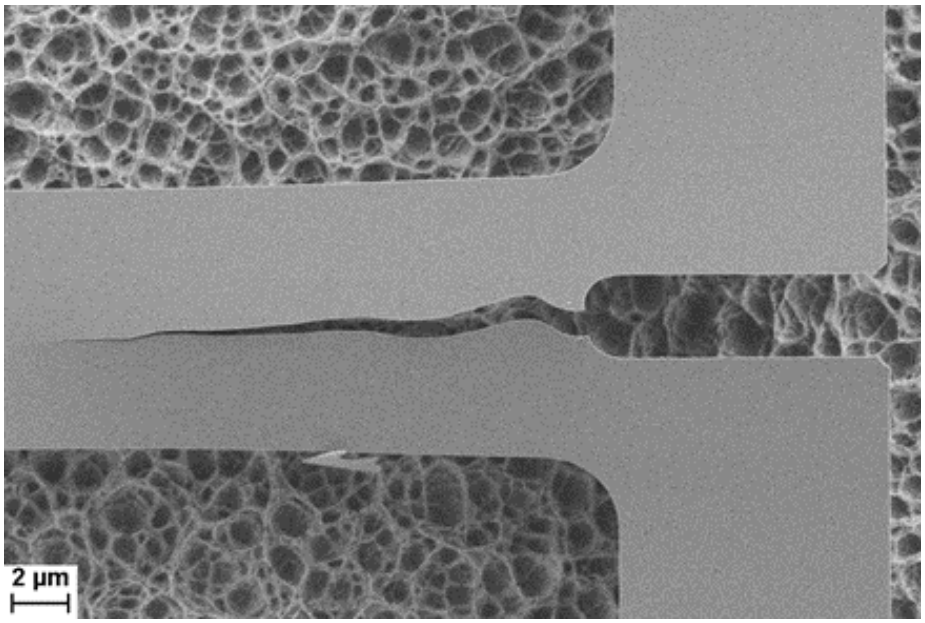

(b)

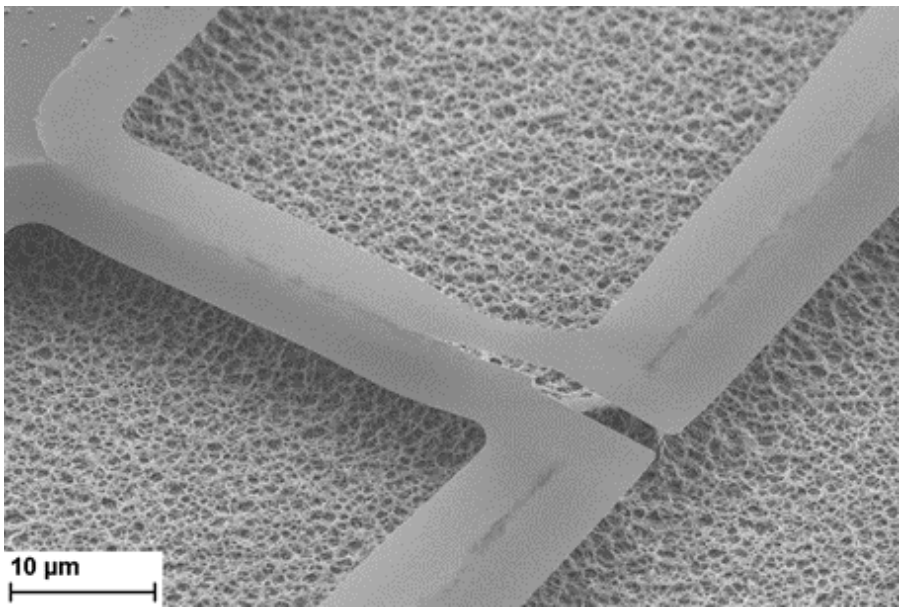

(c)

Figure 14. Examples of successful test structures with arrested crack, (a) structure I, inset a zoomed view of the crack tip, (b) structure VI and (c) a 3D view of structure II. The details about these structures are given in the text.